PHYSICAL REVIEW D **86,** 092007 (2012)

Measurement of $\gamma\gamma^* \to \pi^0$ transition form factor at Belle

S. Uehara,[8] Y. Watanabe,[17] H. Nakazawa,[31] I. Adachi,[8] H. Aihara,[52] D. M. Asner,[38] T. Aushev,[15] A. M. Bakich,[46] K. Belous,[14] V. Bhardwaj,[30] B. Bhuyan,[10] M. Bischofberger,[30] A. Bondar,[1] G. Bonvicini,[57] A. Bozek,[34] M. Bračko,[25,16] T. E. Browder,[7] M.-C. Chang,[4] A. Chen,[31] P. Chen,[33] B. G. Cheon,[6] K. Chilikin,[15] I.-S. Cho,[59] K. Cho,[19] Y. Choi,[45] J. Dalseno,[26,48] Z. Doležal,[2] Z. Drásal,[2] S. Eidelman,[1] D. Epifanov,[1] J. E. Fast,[38] M. Feindt,[18] V. Gaur,[47] N. Gabyshev,[1] Y. M. Goh,[6] B. Golob,[23,16] J. Haba,[8] K. Hayasaka,[29] H. Hayashii,[30] Y. Horii,[29] Y. Hoshi,[50] W.-S. Hou,[33] H. J. Hyun,[21] T. Iijima,[29,28] A. Ishikawa,[51] R. Itoh,[8] M. Iwabuchi,[59] Y. Iwasaki,[8] T. Iwashita,[30] T. Julius,[27] J. H. Kang,[59] T. Kawasaki,[36] C. Kiesling,[26] H. J. Kim,[21] H. O. Kim,[21] J. B. Kim,[20] J. H. Kim,[19] K. T. Kim,[20] M. J. Kim,[21] Y. J. Kim,[19] B. R. Ko,[20] S. Koblitz,[26] P. Kodyš,[2] S. Korpar,[25,16] R. T. Kouzes,[38] P. Križan,[23,16] P. Krokovny,[1] A. Kuzmin,[1] Y.-J. Kwon,[59] J. S. Lange,[5] S.-H. Lee,[20] J. Li,[44] Y. Li,[56] J. Libby,[11] C.-L. Lim,[59] C. Liu,[43] Y. Liu,[3] Z. Q. Liu,[12] D. Liventsev,[15] R. Louvot,[22] D. Matvienko,[1] K. Miyabayashi,[30] H. Miyata,[36] Y. Miyazaki,[28] G. B. Mohanty,[47] A. Moll,[26,48] T. Mori,[28] N. Muramatsu,[41] Y. Nagasaka,[9] E. Nakano,[37] M. Nakao,[8] Z. Natkaniec,[34] S. Nishida,[8] K. Nishimura,[7] O. Nitoh,[55] S. Ogawa,[49] T. Ohshima,[28] S. Okuno,[17] S. L. Olsen,[44,7] Y. Onuki,[52] P. Pakhlov,[15] G. Pakhlova,[15] H. K. Park,[21] K. S. Park,[45] T. K. Pedlar,[24] R. Pestotnik,[16] M. Petrič,[16] L. E. Piilonen,[56] K. Prothmann,[26,48] M. Röhrken,[18] S. Ryu,[44] H. Sahoo,[7] K. Sakai,[8] Y. Sakai,[8] T. Sanuki,[51] Y. Sato,[51] V. Savinov,[40] O. Schneider,[22] C. Schwanda,[13] R. Seidl,[42] K. Senyo,[58] O. Seon,[28] M. E. Sevior,[27] M. Shapkin,[14] C. P. Shen,[28] T.-A. Shibata,[53] J.-G. Shiu,[33] B. Shwartz,[1] A. Sibidanov,[46] F. Simon,[26,48] J. B. Singh,[39] P. Smerkol,[16] Y.-S. Sohn,[59] A. Sokolov,[14] E. Solovieva,[15] M. Starič,[16] T. Sumiyoshi,[54] Y. Teramoto,[37] K. Trabelsi,[8] T. Tsuboyama,[8] M. Uchida,[53] Y. Unno,[6] S. Uno,[8] Y. Usov,[1] P. Vanhoefer,[26] G. Varner,[7] A. Vinokurova,[1] V. Vorobyev,[1] C. H. Wang,[32] P. Wang,[12] M. Watanabe,[36] K. M. Williams,[56] E. Won,[20] Y. Yamashita,[35] C. Z. Yuan,[12] C. C. Zhang,[12] Z. P. Zhang,[43] V. Zhilich,[1] V. Zhulanov,[1] and A. Zupanc[18]

(Belle Collaboration)

[1]*Budker Institute of Nuclear Physics SB RAS and Novosibirsk State University, Novosibirsk 630090*
[2]*Faculty of Mathematics and Physics, Charles University, Prague*
[3]*University of Cincinnati, Cincinnati, Ohio 45221*
[4]*Department of Physics, Fu Jen Catholic University, Taipei*
[5]*Justus-Liebig-Universität Gießen, Gießen*
[6]*Hanyang University, Seoul*
[7]*University of Hawaii, Honolulu, Hawaii 96822*
[8]*High Energy Accelerator Research Organization (KEK), Tsukuba*
[9]*Hiroshima Institute of Technology, Hiroshima*
[10]*Indian Institute of Technology Guwahati, Guwahati*
[11]*Indian Institute of Technology Madras, Madras*
[12]*Institute of High Energy Physics, Chinese Academy of Sciences, Beijing*
[13]*Institute of High Energy Physics, Vienna*
[14]*Institute of High Energy Physics, Protvino*
[15]*Institute for Theoretical and Experimental Physics, Moscow*
[16]*J. Stefan Institute, Ljubljana*
[17]*Kanagawa University, Yokohama*
[18]*Institut für Experimentelle Kernphysik, Karlsruher Institut für Technologie, Karlsruhe*
[19]*Korea Institute of Science and Technology Information, Daejeon*
[20]*Korea University, Seoul*
[21]*Kyungpook National University, Taegu*
[22]*École Polytechnique Fédérale de Lausanne (EPFL), Lausanne*
[23]*Faculty of Mathematics and Physics, University of Ljubljana, Ljubljana*
[24]*Luther College, Decorah, Iowa 52101*
[25]*University of Maribor, Maribor*
[26]*Max-Planck-Institut für Physik, München*
[27]*University of Melbourne, School of Physics, Victoria 3010*
[28]*Graduate School of Science, Nagoya University, Nagoya*
[29]*Kobayashi-Maskawa Institute, Nagoya University, Nagoya*
[30]*Nara Women's University, Nara*
[31]*National Central University, Chung-li*
[32]*National United University, Miao Li*

[33]*Department of Physics, National Taiwan University, Taipei*
[34]*H. Niewodniczanski Institute of Nuclear Physics, Krakow*
[35]*Nippon Dental University, Niigata*
[36]*Niigata University, Niigata*
[37]*Osaka City University, Osaka*
[38]*Pacific Northwest National Laboratory, Richland, Washington 99352*
[39]*Panjab University, Chandigarh*
[40]*University of Pittsburgh, Pittsburgh, Pennsylvania 15260*
[41]*Research Center for Nuclear Physics, Osaka University, Osaka*
[42]*RIKEN BNL Research Center, Upton, New York 11973*
[43]*University of Science and Technology of China, Hefei*
[44]*Seoul National University, Seoul*
[45]*Sungkyunkwan University, Suwon*
[46]*School of Physics, University of Sydney, NSW 2006*
[47]*Tata Institute of Fundamental Research, Mumbai*
[48]*Excellence Cluster Universe, Technische Universität München, Garching*
[49]*Toho University, Funabashi*
[50]*Tohoku Gakuin University, Tagajo*
[51]*Tohoku University, Sendai*
[52]*Department of Physics, University of Tokyo, Tokyo*
[53]*Tokyo Institute of Technology, Tokyo*
[54]*Tokyo Metropolitan University, Tokyo*
[55]*Tokyo University of Agriculture and Technology, Tokyo*
[56]*CNP, Virginia Polytechnic Institute and State University, Blacksburg, Virginia 24061*
[57]*Wayne State University, Detroit, Michigan 48202*
[58]*Yamagata University, Yamagata*
[59]*Yonsei University, Seoul*

(Received 14 May 2012; published 9 November 2012)

We report a measurement of the process $\gamma\gamma^* \to \pi^0$ with a 759 fb^{-1} data sample recorded with the Belle detector at the KEKB asymmetric-energy e^+e^- collider. The pion transition form factor, $F(Q^2)$, is measured for the kinematical region 4 GeV$^2 \lesssim Q^2 \lesssim 40$ GeV^2, where $-Q^2$ is the invariant-mass squared of a virtual photon. The measured values of $Q^2|F(Q^2)|$ agree well with the previous measurements below $Q^2 \simeq 9$ GeV^2 but do not exhibit the rapid growth in the higher Q^2 region seen in another recent measurement, which exceeds the asymptotic QCD expectation by as much as 50%.

DOI: 10.1103/PhysRevD.86.092007 PACS numbers: 14.40.Be, 12.38.Qk, 13.40.Gp

I. INTRODUCTION

Recently, the *BaBar* Collaboration reported a measurement of the photon-pseudoscalar meson (P) transition form factors (TFF) from the process $\gamma\gamma^* \to P$ in the reaction $e^+e^- \to (e)eP$, where $P = \pi^0$ [1] (Fig. 1), η or η' [2], and (e) and e denote an untagged and tagged electron or positron, respectively. The momentum transfer Q^2 (where $-Q^2$ is the squared invariant mass of a spacelike photon) explored by *BaBar* extends up to $\sim$40 GeV^2 compared to the previous measurements by CELLO for $Q^2 < 2.5$ GeV^2 [3] and by CLEO for $Q^2 < 9$ GeV^2 [4]. While the Q^2 dependence of TFFs measured by *BaBar* for the η and η' agrees fairly well with theoretical expectations, that for the π^0 shows rapid growth for $Q^2 > 10$ GeV^2.

Lepage and Brodsky pointed out the importance of TFF measurements more than 30 years ago and proposed tests of perturbative QCD (pQCD) in various exclusive processes [5]. We focus our discussion on the TFF for the pion, that for the η or η' is quite similar. To leading order in the QCD coupling constant, $\alpha_s(Q^2)$, the TFF can be written in the factorized form [6]

$$F(Q^2) = \frac{\sqrt{2} f_\pi}{3} \int_0^1 dx T_H(x, Q^2, \mu, \alpha_s(\mu)) \phi_\pi(x, \mu), \quad (1)$$

where $f_\pi \simeq 0.131$ GeV is the pion decay constant, x is the fraction of momentum carried by a quark (q) or antiquark ($\bar{q}$) in the parent pion, $T_H(x, Q^2, \mu, \alpha_s(\mu))$ is the hard-scattering amplitude for $\gamma\gamma^* \to q\bar{q}$ (Fig. 1), μ is the renormalization scale, and $\phi_\pi(x, \mu)$ is the leading-twist pion distribution amplitude (DA) at x and μ. Note that the pion DA is a universal function and, once determined, describes leading terms in all hard exclusive processes involving a pion. The most prominent examples are the pion electromagnetic form factor and the weak semileptonic decay rate, $B^\pm \to \pi^0 \ell^\pm \nu_\ell$ [6].

At sufficiently high Q^2, Eq. (1) can be written as [6]

$$F(Q^2) = \frac{\sqrt{2} f_\pi}{3} \int_0^1 dx \frac{\phi_\pi(x)}{xQ^2} + \mathcal{O}(1/Q^4). \quad (2)$$

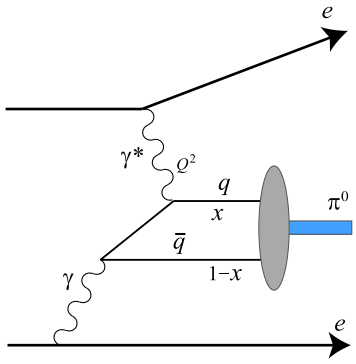

FIG. 1 (color online). A Feynman diagram for $\gamma\gamma^* \to q\bar{q} \to \pi^0$ in e^+e^- collisions.

Because the asymptotic pion DA is $\phi_\pi^{\rm asy} = 6x(1-x)$, it follows that $Q^2F(Q^2)$ at $Q^2 \to \infty$ is exactly normalized as [5]

$$Q^2F(Q^2) = \sqrt{2}f_\pi \simeq 0.185 \text{ GeV}. \quad (3)$$

The measurements reported by CELLO [3] and CLEO [4] support this prediction; the measured values seem to approach this asymptotic value from below. The recent measurement by *BaBar* [1] has changed this situation drastically. The measured $Q^2|F(Q^2)|$ values seem to increase with Q^2, exceeding the QCD asymptotic value by as much as 50%; this has created excitement and renewed interest in this quantity.

Many theoretical constructs have been made to explain this Q^2 dependence. Early attempts pointed out that the *BaBar* result requires a nearly flat pion DA (e.g., [7,8]), which implies that the pion behaves as a pointlike particle. The conclusions of the theoretical analyses can be divided into two groups: those that can explain the *BaBar* result (e.g., [6,9]) and those that cannot (e.g., [10,11]).

This theoretical controversy seems to have been settled by a recent analysis of Brodsky, Cao, and de Téramond [12], who investigated TFFs of the π^0, η, and η' using four typical models of the meson DA. They concluded that the rapid growth of the π^0 TFF with Q^2 at *BaBar*, together with the gentle Q^2 dependence of the η and η' TFFs also measured at *BaBar* are difficult to explain within the present framework of QCD. They also pointed out drawbacks of earlier theoretical attempts that explained the Q^2 dependence of the π^0 TFF at *BaBar* and stated that the *BaBar* π^0 result, if confirmed, would imply new physics beyond standard QCD.

In this article, we report an independent measurement of the π^0 TFF in the Q^2 region of interest.

II. EXPERIMENTAL APPARATUS AND EVENT SELECTION

We briefly describe the Belle detector and then give a description of the event selection. Finally, we present some event distributions to illustrate the selection criteria.

A. The Belle detector and data sample

We use a 759 fb^{-1} data sample recorded with the Belle detector at the KEKB asymmetric-energy e^+e^- collider [13]. We combine data samples collected at several beam energies: at the $\Upsilon(4S)$ resonance ($\sqrt{s} = 10.58$ GeV) and 60 MeV below it (637 fb^{-1} in total), at the $\Upsilon(3S)$ resonance ($\sqrt{s} = 10.36$ GeV, 3.2 fb^{-1}), and near the $\Upsilon(5S)$ resonance ($\sqrt{s} = 10.88$ GeV, 119 fb^{-1}). When combining the data, the slight dependence of the two-photon cross sections on beam energy is properly taken into account.

This analysis is performed in the "single-tag" mode, where either the recoil electron or positron (hereafter referred to as electron) alone is detected. We restrict the virtuality (Q^2) of the untagged-side photon to be small by imposing a strict transverse-momentum balance with respect to the beam axis for the tagged electron and the final-state neutral pion. In this article, we refer to events tagged by an e^+ or an e^- as "p-tag" (positron-tag) or "e-tag" (electron-tag), respectively.

1. Belle detector

A comprehensive description of the Belle detector is given elsewhere [14]. We mention here only the detector components essential for this measurement. Charged tracks are reconstructed from the drift-time information in a central drift chamber (CDC) located in a uniform 1.5 T solenoidal magnetic field. The z axis of the detector and the solenoid are along the positron beam direction, with the positron beam pointing in the $-z$ direction. The CDC measures the longitudinal and transverse-momentum components, i.e., along the z axis and in the $r\varphi$ plane perpendicular to the beam, respectively. Track trajectory coordinates near the collision point are provided by a silicon vertex detector. Photon detection and energy measurements are performed with a CsI(Tl) electromagnetic calorimeter (ECL). Electron identification (ID) is based on E/p, the ratio of the calorimeter energy and the track momentum. We employ this rather simple variable because the background from hadrons and muons is small compared to the dominant radiative Bhabha and two-photon background contributions.

2. Data sample

To be recorded, events must satisfy one of the two mutually exclusive triggers based on ECL energy: the HiE (high-energy threshold) trigger and the CsiBB (ECL-Bhabha) trigger [15]. The HiE trigger requires that the sum of the energies measured by the ECL in an event exceed 1.15 GeV but that the event not be Bhabha-like; the HiE trigger is vetoed by the CsiBB trigger. The CsiBB trigger is designed to identify back-to-back Bhabha events [15] and is prescaled to reduce their high rate. For the purpose of monitoring trigger performance, the events triggered by the CsiBB are recorded once per 50 CsiBB

triggers (i.e., are prescaled by a factor of 50). This prescaled event sample has been extensively used in our analysis to select a subsample of signal events, and to calibrate and test the trigger simulation for the CsiBB veto implemented in the HiE trigger.

We do not use information on track triggers because they require two or more charged tracks; our signal has only one charged track.

B. Single-track skim

To simplify the logistics of the data analysis, we use a "single-track" skim whose requirements are the following.

(S1) The event is triggered by the HiE or the CsiBB trigger.

(S2) There is only one track that satisfies $p_t > 0.5$ GeV/c, $-0.8660 < \cos\theta < 0.9563$, $dr < 1$ cm, and $|dz| < 5$ cm. There are no other tracks that satisfy $p_t > 0.1$ GeV/c and $dr < 5$ cm, $|dz| < 5$ cm in the entire CDC volume. Here, p_t is the transverse momentum in the laboratory frame with respect to the positron beam axis, θ is the polar angle of the momentum direction with respect to the z axis, and (dr, dz) are the cylindrical coordinates of the closest approach of the track to the beam axis.

(S3) There are one or more neutral clusters in the ECL, whose energy sum is greater than 0.5 GeV.

These conditions are efficient in selecting a signal process within the kinematical regions of $e^+e^- \to (e)e\pi^0$ in which one electron escapes detection at small forward angles. They also select radiative-Bhabha $[e^+e^- \to (e)e\gamma]$ events with a virtual Compton (VC) process configuration, in which one of the electrons escapes detection in the forward direction; such events are used for trigger calibration.

C. Selection criteria for signal candidate events

A signal event consists of an energetic electron and two photons as described below. Candidate events are selected from the single-track skim with the following selection criteria. The kinematical variables are calculated in the laboratory system unless otherwise noted; those in the e^+e^- center-of-mass (c.m.) frame are identified with an asterisk.

(1) Events are triggered by the HiE trigger. We also use events triggered by the CsiBB trigger, separately, for the $Q^2 = 4$–6 GeV^2 region of the e-tag.

(2) There is exactly one track as required in the skim condition (S2).

(3) For electron ID, we require $E/p > 0.8$ for the candidate electron track.

(4) The absolute value of the momentum of the electron is greater than 1.0 GeV/c, where the electron energy is corrected for photon radiation or bremsstrahlung in the following way. In a 3° cone around the track, we collect all photons in the range 0.1 GeV $< E_\gamma < p_e/3$, where p_e is the measured absolute momentum of the electron track. The absolute momentum of the electron is replaced by $p_e + \Sigma E_\gamma$.

(5) We require exactly two photons above 0.2 GeV, excluding those used for bremsstrahlung and final-state radiation recovery in (4). We designate the energies of the two photons by $E_{\gamma 1}$ for the higher and $E_{\gamma 2}$ for the lower.

(6) When there are one or more extra photons with energy greater than 0.05 GeV, we require that there be no π^0 candidate reconstructed with a two-photon combination different from the pair in (5) in the following way. We search for a π^0 candidate reconstructed from two photons that satisfies a goodness-of-fit criterion, $\chi^2 < 9$, in a π^0-mass-constrained fit. If we find such a π^0 (including the case when only one photon in (5) is shared in the π^0), the event is rejected.

(7) The two-photon energy sum $E_{\gamma\gamma}$ defined as

$$E_{\gamma\gamma} = E_{\gamma 1} + E_{\gamma 2} \tag{4}$$

satisfies $E_{\gamma\gamma} > 1.0$ GeV.

(8) The cosines of the polar angles for the electron (θ_e) and the two photons ($\theta_{\gamma 1}$ and $\theta_{\gamma 2}$) must be within the range $-0.6235 < \cos\theta_i < 0.9481$ ($i = e$, $\gamma 1$, or $\gamma 2$). This is the sensitive region for the HiE trigger.

(9) We reject events with a polar-angle combination $(\cos\theta_e, \cos\theta_{\gamma\gamma})$ that falls in the predetermined two-dimensional angular area shown in Fig. 2, where $\theta_{\gamma\gamma}$ is the polar angle of the momentum

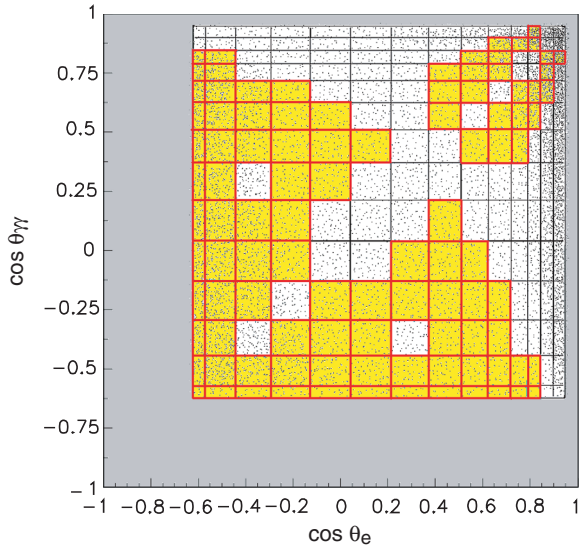

FIG. 2 (color). Two-dimensional angular regions in $(\cos\theta_e, \cos\theta_{\gamma\gamma})$ defined as the Bhabha mask (see Appendix A for the details). Events in the yellow (white) regions are selected (rejected). The gray region is outside of the angular acceptance. The mask is symmetric for e and $\gamma\gamma$. The scattered dots in the figure show signal Monte Carlo simulation events without the Bhabha veto applied.

summed for the two photons. This rejection is referred to as the "Bhabha-mask" rejection. The Bhabha mask is introduced to limit the fiducial region to a range where the efficiency of the HiE trigger is well determined. The details of the Bhabha mask are given in Appendix A.

(10) The energy asymmetry for the two photons, defined as

$$E_{\rm asym} = \frac{E_{\gamma 1} - E_{\gamma 2}}{E_{\gamma\gamma}} \tag{5}$$

satisfies $E_{\rm asym} < 0.8$ to eliminate low-energy background photons.

(11) The polar-angle difference, $\Delta\theta = |\theta_{\gamma 1} - \theta_{\gamma 2}|$, for the two photons multiplied by $E_{\gamma\gamma}$ satisfies

$$E_{\gamma\gamma}\Delta\theta > 0.18 \text{ radian} \cdot \text{GeV}. \tag{6}$$

This rejects the large background from radiative-Bhabha events with a conversion, i.e. $e^+e^- \to (e)e\gamma$, $\gamma \to e^+e^-$, where the electron-positron pair from a photon conversion tends to separate in a common plane perpendicular to the magnetic field (which is along the z axis), and the e^+e^- pair is misreconstructed as a $\gamma\gamma$ candidate.

(12) We exploit the charge-direction correlation ("right-sign") for the single-tag two-photon process between the electric charge of the tagged electron ($q_{\rm tag}$) and the z component of the momentum of the $e\gamma\gamma$ system in the e^+e^- c.m. frame by requiring

$$q_{\rm tag} \times (p^*_{z,e} + p^*_{z,\gamma\gamma}) < 0. \tag{7}$$

(13) We require $0.85 < E_{\rm ratio} < 1.1$, where

$$E_{\rm ratio} = \frac{E^{*\rm measured}_{\gamma\gamma}}{E^{*\rm expected}_{\gamma\gamma}}. \tag{8}$$

This requirement is motivated by a three-body kinematical calculation for $e^+e^- \to (e)e\pi^0$, imposing a four-momentum conservation condition $p_{\rm initial}(e^+e^-) = p_{\rm final}((e)e\gamma\gamma)$ wherein the direction of the π^0 momentum is taken to be parallel to that of the observed $\gamma\gamma$ system in the e^+e^- c.m. frame. The expected $E^*_{\gamma\gamma}$ value is obtained by assigning the nominal π^0 mass to the $\gamma\gamma$ system. This calculation is not sensitive to the input $\gamma\gamma$ invariant mass.

(14) We reject events with a back-to-back configuration in the e^+e^- c.m. frame, to eliminate backgrounds from Bhabha events in which a track is not reconstructed; we require $\zeta^*(e, \gamma\gamma) < 177°$, where $\zeta^*(e, \gamma\gamma)$ is the opening angle between the electron and the $\gamma\gamma$ system.

(15) We require the electron and the $\gamma\gamma$ system to be nearly back-to-back when their momentum directions are projected onto the $r\varphi$ plane: $\alpha(e, \gamma\gamma) < 0.1$ radians, where the acoplanarity angle α is defined as the difference between the opening angle of the two directions on the projected plane and π.

(16) We require transverse-momentum balance in the e^+e^- c.m. frame, $|\Sigma \boldsymbol{p}^*_t| < 0.2$ GeV/c, where

$$|\Sigma \boldsymbol{p}^*_t| = |\boldsymbol{p}^*_{t,e} + \boldsymbol{p}^*_{t,\gamma\gamma}|. \tag{9}$$

With the above selection criteria, we collect $e^+e^- \to (e)e\gamma\gamma$ candidates in the broad $\gamma\gamma$ invariant-mass range of $0.07\ \text{GeV}/c^2 \lesssim M_{\gamma\gamma} \lesssim 0.50\ \text{GeV}/c^2$. The minimum $\gamma\gamma$ invariant mass is determined mainly by selection criteria (7) and (11) on $E_{\gamma\gamma}$ and $E_{\gamma\gamma}\Delta\theta$. We do not apply any explicit selection on $M_{\gamma\gamma}$ for the determination of the π^0 signal yield. Instead, we later obtain the π^0 yield by fitting the $M_{\gamma\gamma}$ distribution in Q^2 bins

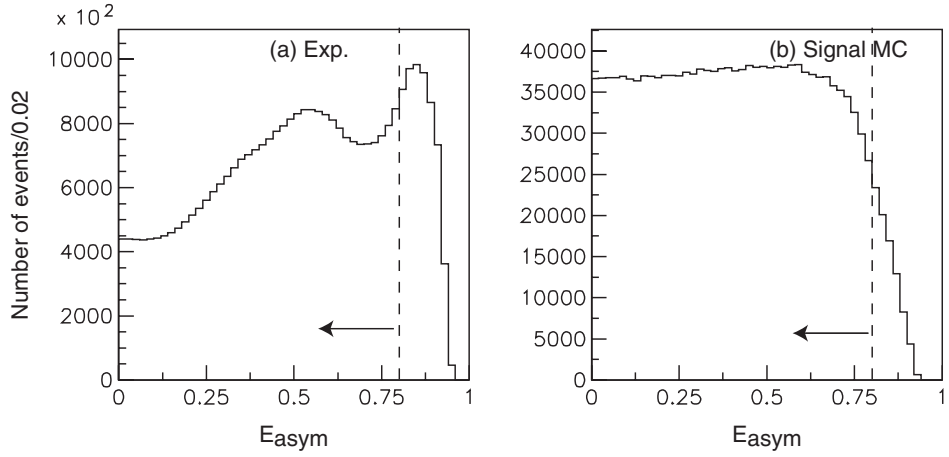

FIG. 3. Energy asymmetry [$E_{\rm asym}$, defined in selection criterion (10)] for the two-photon candidates for events in which p_e, $E_{\gamma\gamma}$, and $\theta_{\gamma\gamma}$ satisfy the criteria for (a) experimental data and (b) signal Monte Carlo samples. The dashed lines show the selection boundaries. Arrows indicate the accepted regions.

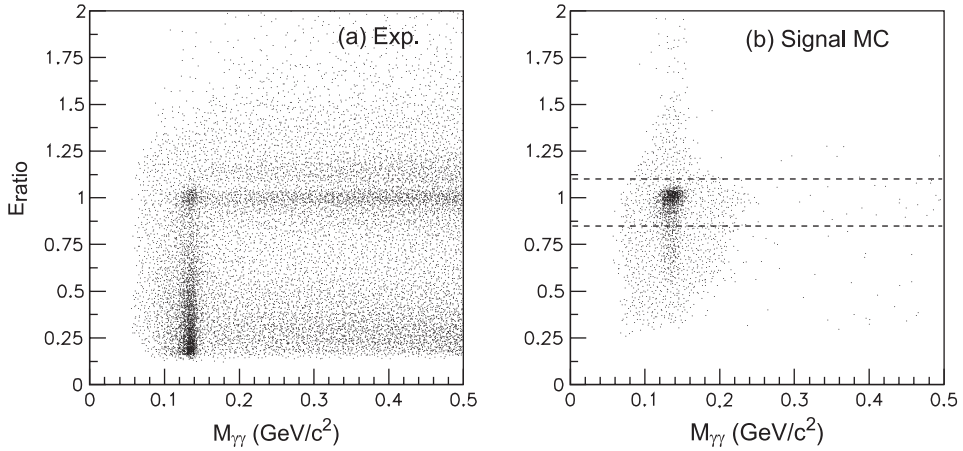

FIG. 4. Scatter plots for $E_{\rm ratio}$ versus $M_{\gamma\gamma}$ for (a) experimental data and (b) signal MC samples. See the text for the selection conditions. The horizontal band between the dashed lines in (b) is the accepted region.

separately for the p-tag and e-tag samples: the selection requirements for the two tags are very different because the beam energies and the detector are asymmetric.

D. Event distributions

In this subsection, we illustrate how the signal candidates are selected. Figure 3 shows the energy asymmetry [$E_{\rm asym}$, defined in criterion (10)] of the two photons for events in which the electron and photons satisfy the selection criteria for momenta, energies, and angles. Events with a large asymmetry are suppressed by the minimum photon energy requirement (0.2 GeV), yet a peak at $E_{\rm asym} > 0.8$ is still visible in the data from low-energy photon background [Fig. 3(a)].

Figures 4 and 5 show $E_{\rm ratio}$ versus $M_{\gamma\gamma}$ and $|\Sigma \boldsymbol{p}_t^*|$, respectively, for the samples after applying selection criteria (11) and (15) for $E_{\gamma\gamma}\Delta\theta$ and the acoplanarity angle, respectively. The latter is plotted only for events in the vicinity of the pion mass, $0.120\ {\rm GeV}/c^2 < M_{\gamma\gamma} < 0.145\ {\rm GeV}/c^2$, where the $E_{\rm ratio}$ requirement is not applied. We find a significant enhancement in the signal region of the experimental data near $E_{\rm ratio} = 1$, $M_{\gamma\gamma} = m_\pi$, and $|\Sigma \boldsymbol{p}_t^*| = 0$, where m_π is the nominal π^0 mass. A narrow enhancement in the experimental data around $E_{\rm ratio} = 1.15$ [Fig. 4(a)] is due to background from radiative-Bhabha events and is reproduced by the background Monte Carlo (MC). The signal in the experimental data is well separated from the low-energy π^0 background in the region near $|\Sigma \boldsymbol{p}_t^*| = 0$ (Fig. 5).

In Fig. 6, we show the scatter plot for $E_{\gamma\gamma}\Delta\theta$ versus $M_{\gamma\gamma}$ for the final samples in the range $15\ {\rm GeV}^2 < Q^2 < 40\ {\rm GeV}^2$, where only the corresponding selection criterion is not applied. The large background from radiative-Bhabha events is present primarily in the range $0.05\ {\rm GeV}/c^2 \lesssim M_{\gamma\gamma} \lesssim 0.20\ {\rm GeV}/c^2$ below the selected boundary in

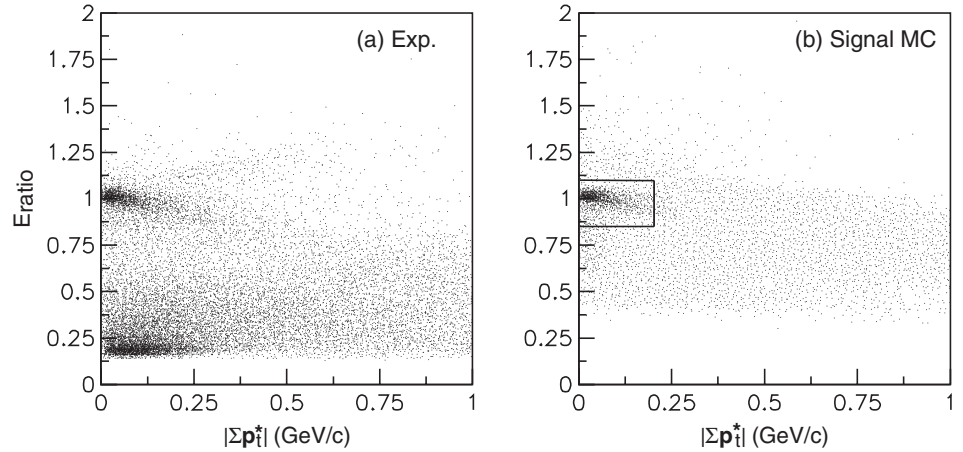

FIG. 5. Scatter plots for $E_{\rm ratio}$ versus $|\Sigma \boldsymbol{p}_t^*|$ for the (a) experimental data and (b) signal MC samples. See the text for the selection requirements. The solid box in (b) shows the selection region.

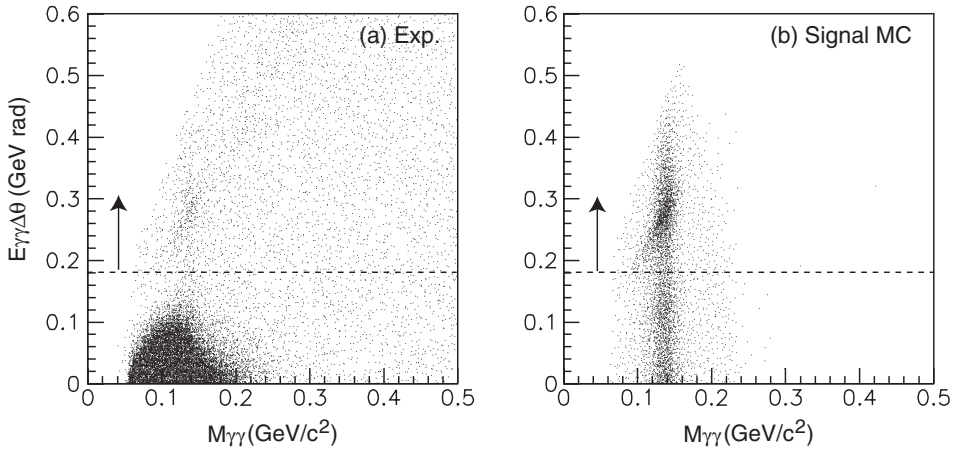

FIG. 6. Scatter plots for $E_{\gamma\gamma}\Delta\theta$ versus $M_{\gamma\gamma}$ for (a) the experimental data and (b) signal MC samples. This distribution is for the final samples in the range 15 GeV$^2 < Q^2 <$ 40 GeV^2 where only the $E_{\gamma\gamma}\Delta\theta$ criterion is not applied. The dashed lines show the selection boundaries. Arrows show the accepted regions.

$E_{\gamma\gamma}\Delta\theta$, with no contamination seen above the boundary. This background is discussed in more detail in Sec. IV B.

III. SIGNAL MONTE CARLO AND ESTIMATION OF THE DETECTION EFFICIENCIES

In this analysis, MC programs play an essential role in defining the selection criteria and determining the detection efficiencies. In this section, a specially developed signal MC program is described. The efficiency determination is then described. A detailed discussion of the trigger simulator tuning is given in Appendix B, where radiative-Bhabha events are compared with MC events generated by Rabhat [16]. This MC is a specially developed program to deal with the VC process in which an electron is scattered forward and remains undetected.

A. Signal Monte Carlo, TREPSBST

To calculate the conversion factor between the transition form factor and the differential cross section, to estimate the overall efficiency using signal MC events and to perform other studies, an MC program, TREPSBST, was developed for the signal process $e^+e^- \to (e)e\pi^0$.

TREPSBST implements the formulas of Eqs. (2.1) and (4.5) in Ref. [17] and is based on the MC program TREPS [18], which was modified to match the condition that the equivalent photon approximation is not applied. In TREPSBST, we always retain the condition $Q_1^2 > Q_2^2$ for virtuality of the two colliding photons by requiring $Q_1^2 >$ 3.0 GeV^2 and $Q_2^2 <$ 1.0 GeV^2 for the ranges of integration and event generation.

This Q_2^2 range is sufficient to generate signal events over the kinematical region for the $|\Sigma \boldsymbol{p}_t^*|$ selection criterion, and is also used to define the differential cross section $d\sigma/dQ^2$ for the signal process in this analysis (see Sec. V C).

The program calculates the differential cross section $d\sigma/dQ_1^2$ for the given Q_1^2 points and, separately, generates MC events with a specified Q_1^2 distribution. The shape of the distribution, in principle, does not affect the efficiency determination, which is evaluated for each Q_1^2 bin with a bin width of 1 GeV^2. However, we assign a systematic error from the uncertainty in the Q^2-dependence effect for some bins in the lowest Q^2 region (see Sec. V E).

The differential cross section for the signal process is calculated at tree level assuming a g^2 coupling parameter derived from $\Gamma_{\gamma\gamma} = 8$ eV [defined for real photons as in Eq. (12) below]. Both the transition form factor squared $|F(Q^2)|^2$ and differential cross section $d\sigma/dQ^2$ are proportional to the parameter g^2, and thus their ratio

$$2A(Q^2) = \frac{d\sigma/dQ^2}{|F(Q^2)|^2}, \tag{10}$$

which has to be used to convert the measured differential cross section to the form factor, is not affected by the assumed $\Gamma_{\gamma\gamma}$ value [17]. In Eq. (10), we explicitly include a factor of 2 to show the contributions from both p- and e-tags to the coefficient. The transition form factor $F(Q^2)$ is defined as

$$|F(Q^2)|^2 = \lim_{Q_2^2 \to 0} |F(Q^2, Q_2^2)|^2. \tag{11}$$

The normalization of the form factor $F(Q^2, Q_2^2)$ is defined based on the relation in Ref. [4], where it is extrapolated to the real two-photon coupling ($\gamma\gamma \to \pi^0$),

$$|F(0,0)|^2 = \frac{1}{(4\pi\alpha)^2} \frac{64\pi\Gamma_{\gamma\gamma}}{m_\pi^3}; \tag{12}$$

here α is the fine structure constant and $\Gamma_{\gamma\gamma}$ is the two-photon decay width for the neutral pion.

A calculation of the conversion factor $2A(Q^2)$ requires a threefold numerical integration, which is performed over

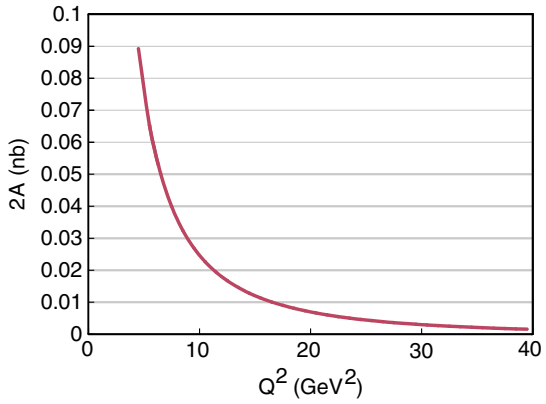

FIG. 7 (color online). Calculated $2A(Q^2)$ function for $\sqrt{s} = 10.58$ GeV.

the following variables: Q_2^2, the photon energy of the small-Q^2 side (ω_2), and the acoplanarity for the two colliding virtual photons ($\Delta\varphi$). The choice of kinematical variables is discussed in Ref. [19].

We use the following assumption to extend the form factor to nonzero Q_2^2:

$$|F(Q_1^2, Q_2^2)| = \frac{|F(Q_1^2, 0)|}{1 + \frac{Q_2^2}{m_\rho^2}}, \tag{13}$$

where $m_\rho = 0.77$ GeV/c^2. The ratio $2A(Q^2)$ is calculated for the Q^2 range of the present measurement with a step size of 1 GeV^2. Convergence and stability of the numerical integration have been carefully verified to an accuracy of $\sim 10^{-3}$. We have applied spline interpolation for $2A(Q^2)$ when necessary. The results obtained for $2A(Q^2)$ are plotted in Fig. 7 for $\sqrt{s} = 10.58$ GeV, $Q_2^{2\,\max} = 1.0$ GeV^2 and to leading order in QED.

The event generation is performed using the same integrand but including initial-state radiation (ISR) effects from the tag-side electron. Inclusion of ISR changes the kinematics and Q_1^2 significantly. Meanwhile, ISR from the untagged side has little effect because ISR is nearly parallel not only to the initial-state electron but also to the final-state untagged electron. We use an exponentiation technique [20] for the photon emission based on the parameter $\eta = (2\alpha/\pi)(\log(Q_1^2/m_e^2) - 1)$ and the probability density for the photon energy distribution, $dP(r_k) \propto r_k^{\eta-1} dr_k$, where

$$r_k \equiv \frac{E^*_{\rm ISR}}{E^*_{\rm beam}}. \tag{14}$$

As an approximation, the photon is always emitted along the electron direction. We set the maximum fractional energy of radiation $r_k^{\max} = 0.25$. Because events with a large r_k, typically above 0.1, are rejected by selection criterion (13) using $E_{\rm ratio}$ (see Sec. V E 2 and Fig. 23), this value of $r_k^{\max}$ in MC generation is large enough to generate MC events over the selected range. In this configuration, the correction factor $1 + \delta$ to the tree-level cross section from the untagged side is close to unity [21]. Radiation of low-Q^2 virtual photons is strongly suppressed by the emission of ISR in the untagged side.

We generate events with a virtuality of the tagged-side photon Q_1^2 distributed with a constant form factor. The Q_1^2 of each event is modified by ISR. We use the momentum of the ISR photon to estimate the true Q_1^2 value in signal MC events and to study the Q^2 dependence of the detection efficiency.

B. Efficiency determination

The selection efficiency is calculated using the signal MC, the detector simulation (GSIM), and the trigger simulation (TSIM). The efficiency is estimated for each Q^2 bin for p- and e-tags separately. We show the Q^2 dependence of the efficiency for a typical run at the $\Upsilon(4S)$ energy and another at the $\Upsilon(5S)$ energy in Figs. 8 and 9. The overall detection efficiency shown in Fig. 8 includes the trigger efficiency and the Bhabha-mask selection. The trigger

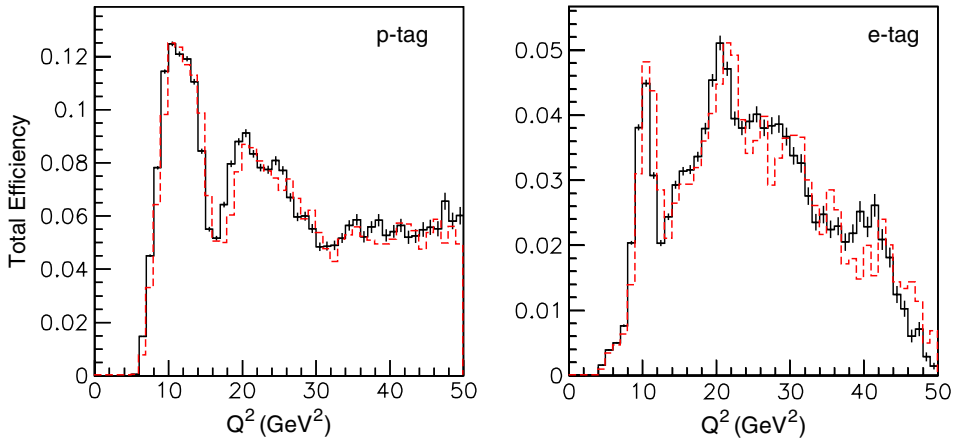

FIG. 8 (color online). The total selection efficiencies as a function of Q^2 determined by MC for runs at the $\Upsilon(4S)$ (solid histogram, where the error bars show statistical errors) and $\Upsilon(5S)$ energies (dashed histogram).

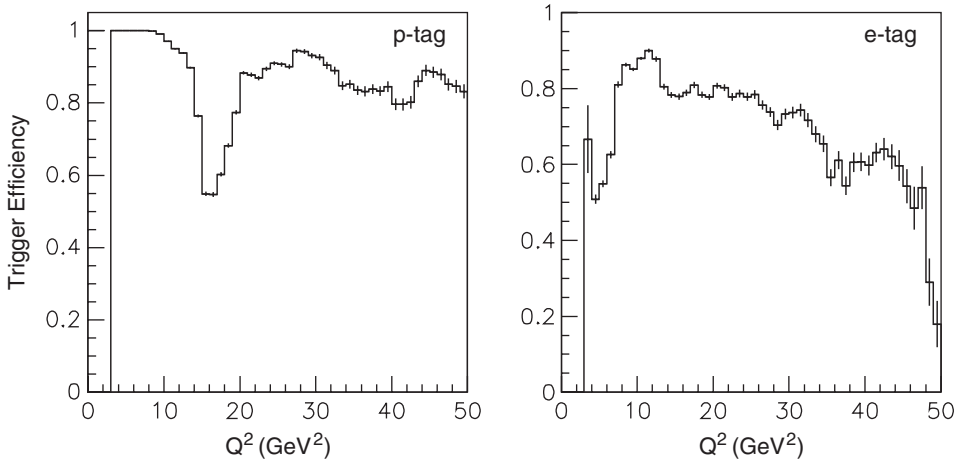

FIG. 9. The trigger efficiencies determined from MC for a typical run at the $\Upsilon(4S)$ energy. The error bars show statistical errors.

efficiency (Fig. 9) is shown within the acceptance region after the Bhabha-mask selection is applied.

A measurement corresponding to these efficiencies is reported only in the region $6\ \mathrm{GeV}^2 < Q^2 < 40\ \mathrm{GeV}^2$, where the HiE trigger with the Bhabha mask is used. The complicated shapes are due to the structure of the Bhabha mask. The efficiencies are obtained for each Q^2 bin, where the value of Q^2 is evaluated using generated

TABLE I. Numbers of reconstructed events (N_{rec}) obtained from the fit to the experimental $M_{\gamma\gamma}$ distribution (Sec. IVA), the number of events after the unfolding (N_{cor}), background fractions and efficiencies for each Q^2 bin, listed separately for p- and e-tags. The first column is the representative Q^2 for that bin [see Eq. (18)]. N_{rec} and N_{cor} include both signal and background yields. Note that the HiE + 50 * CsiBB samples are used for the $Q^2 = 4$–6 GeV^2 bins in the e-tag case.

Q^2 (GeV^2)	Q^2 bin range (GeV^2)	Tag	N_{rec}	N_{cor}	Background (%)	Efficiency
6.47	6.0–7.0	p	140 ± 14	167 ± 17	2.8	0.0134
7.47	7.0–8.0	p	320 ± 21	323 ± 25	2.8	0.0434
8.48	8.0–9.0	p	418 ± 23	426 ± 27	2.8	0.0763
9.48	9.0–10.0	p	379 ± 21	364 ± 25	2.8	0.1120
10.48	10.0–11.0	p	286 ± 19	279 ± 22	2.8	0.1260
11.48	11.0–12.0	p	222 ± 17	222 ± 21	2.8	0.1220
12.94	12.0–14.0	p	259 ± 19	249 ± 22	3.0	0.1150
14.95	14.0–16.0	p	105 ± 13	98 ± 14	3.0	0.0724
16.96	16.0–18.0	p	49 ± 9	49 ± 11	3.0	0.0571
18.96	18.0–20.0	p	52 ± 9	51 ± 12	3.0	0.0819
22.29	20.0–25.0	p	82 ± 13	78 ± 15	3.5	0.0826
27.33	25.0–30.0	p	44 ± 9	44 ± 10	3.5	0.0648
34.46	30.0–40.0	p	8.4 ± 6.8	8.4 ± 6.8	5.0	0.0550
4.46	4.0–5.0	e	656 ± 190	680 ± 197	2.8	0.0231
5.47	5.0–6.0	e	1066 ± 230	1072 ± 231	2.8	0.0630
6.47	6.0–7.0	e	60 ± 9	58 ± 8	2.8	0.0049
7.47	7.0–8.0	e	38.0 ± 7.0	36.9 ± 9.1	2.8	0.0073
8.48	8.0–9.0	e	84 ± 11	93 ± 15	2.8	0.0191
9.48	9.0–10.0	e	149 ± 16	159 ± 21	2.8	0.0365
10.48	10.0–11.0	e	115 ± 13	104 ± 16	2.8	0.0447
11.48	11.0–12.0	e	53 ± 9	45 ± 12	2.8	0.0322
12.94	12.0–14.0	e	39 ± 8	37 ± 10	3.0	0.0224
14.95	14.0–16.0	e	41 ± 8	41 ± 10	3.0	0.0296
16.96	16.0–18.0	e	30.6 ± 7.2	30.5 ± 8.9	3.0	0.0319
18.96	18.0–20.0	e	31.0 ± 7.8	31.7 ± 9.8	3.0	0.0406
22.29	20.0–25.0	e	32.4 ± 9.0	29.2 ± 9.9	3.5	0.0426
27.33	25.0–30.0	e	13.6 ± 6.4	13.1 ± 7.2	3.5	0.0375
34.46	30.0–40.0	e	14.0 ± 5.0	13.4 ± 4.8	5.0	0.0262

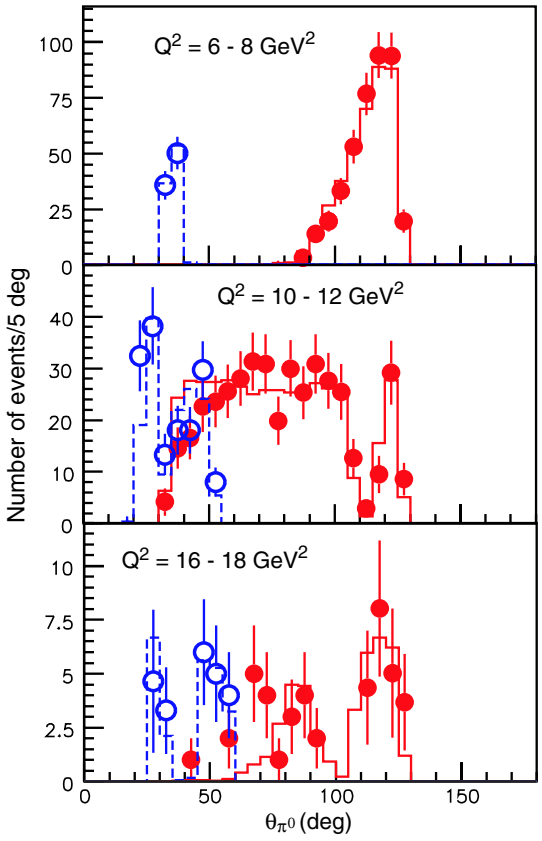

FIG. 10 (color online). Comparison between the π^0 angular distributions in signal candidate events in data (circles) and signal MC (histograms) for different Q^2 regions. Closed (open) circles and solid (dashed) histograms are from events of p-tag (e-tag). In the data, the background contribution is subtracted. The MC events are normalized to the experimental yield after the background subtraction in each Q^2 region.

four-momentum vectors of signal MC events with ISR taken into account. We generated MC samples of 8×10^6 events at $\Upsilon(4S)$ and 2×10^6 events at $\Upsilon(5S)$; these samples correspond, approximately, to an integrated luminosity a few dozen times larger than our data. The efficiency obtained in bins of Q^2 is summarized in Table I.

To validate the efficiency calculation, we compare the distributions for the π^0 laboratory angle in signal candidate events with those from the signal MC samples in different Q^2 regions in Fig. 10. Data events are shown in the range of two-photon invariant mass $0.120\ \mathrm{GeV}/c^2 < M_{\gamma\gamma} < 0.145\ \mathrm{GeV}/c^2$ after subtracting the background that was estimated using the π^0-mass sideband region $0.170\ \mathrm{GeV}/c^2 < M_{\gamma\gamma} < 0.195\ \mathrm{GeV}/c^2$ using the fitting procedure described in Sec. IV A. Qualitative agreement between the data and MC in Fig. 10 confirms the validity of the efficiency calculation based on the signal MC. The validity of this calculation has also been checked in data using a sample of radiative-Bhabha events, which have no trigger bias. The details are described in Appendix B.

IV. EXTRACTION OF THE π^0 YIELD AND BACKGROUND ESTIMATION

In deriving the differential cross section, $d\sigma/dQ^2$, we first extract the π^0 yield in each Q^2 bin by fitting the $M_{\gamma\gamma}$ distribution. Possible backgrounds are then identified, evaluated, and subtracted. These analysis steps are described below.

A. Extraction of the π^0 yield

The π^0 yield is extracted in each Q^2 bin for the p-tag and e-tag samples. For each signal candidate event, Q^2 is calculated using the measured four-momentum of the detected electron (p_e) by

$$Q^2_{\mathrm{rec}} = -(p_{\mathrm{beam}} - p_e)^2 = 2E^*_{\mathrm{beam}}E^*_e(1 + q_{\mathrm{tag}}\cos\theta^*_e), \quad (15)$$

where p_{beam} is the nominal four-momentum of the beam particle with the same charge as the detected electron; the right-hand side is given by the beam energy E^*_{beam} and the observables of the tagged electron in the e^+e^- c.m. frame. We do not apply a correction for ISR on an event-by-event basis; instead, this effect is taken into account in the Q^2 unfolding described in Sec. V A.

Figure 11 shows scatter plots of Q^2 versus $M_{\gamma\gamma}$ for the final experimental samples. After dividing them into Q^2 bins, we fit the $M_{\gamma\gamma}$ distribution in the region $0.08\ \mathrm{GeV}/c^2 < M_{\gamma\gamma} < 0.30\ \mathrm{GeV}/c^2$ to determine the π^0 yield.

To extract this yield, we fit the two-photon invariant-mass distribution with a double Gaussian describing the signal and a quadratic polynomial approximating the background, namely,

$$f(x) = a + bx + cx^2 + \frac{A}{\sqrt{2\pi}\sigma}\left\{re^{-\frac{(x-m)^2}{2\sigma^2}} + \frac{1-r}{k}e^{-\frac{\{x-(m+\Delta m)\}^2}{2(k\sigma)^2}}\right\}, \quad (16)$$

where $x \equiv M_{\gamma\gamma}$, a, b, and c are the background parameters, A is signal yield, and m and σ are the mass and width (i.e., mass resolution), respectively, for the signal. For Q^2 bins with poor statistics, the last two fit parameters are fixed to values estimated from signal MC, as described below. The parameters r, k, and Δm approximate the relative size, width, and position of the two Gaussian components, respectively, and are fixed to values from MC simulation in a Q^2-dependent manner.

In Q^2 bins with low signal statistics, the determination of the width is poor and is significantly correlated with the yield. For such bins, we fix the mass and width parameters to values that are expected from the signal MC, taking into account a small deviation measured using the data: the difference between data and MC is $\delta m \simeq -1\ \mathrm{MeV}/c^2$, whereas the mass resolutions show good agreement. These parameters are fixed in the fit for $Q^2 > 20\ \mathrm{GeV}^2$ for the p-tag, and $Q^2 = 7$–$8\ \mathrm{GeV}^2$ or $Q^2 > 12\ \mathrm{GeV}^2$ for the HiE and $Q^2 < 6\ \mathrm{GeV}^2$ for the CsiBB for the e-tag. The

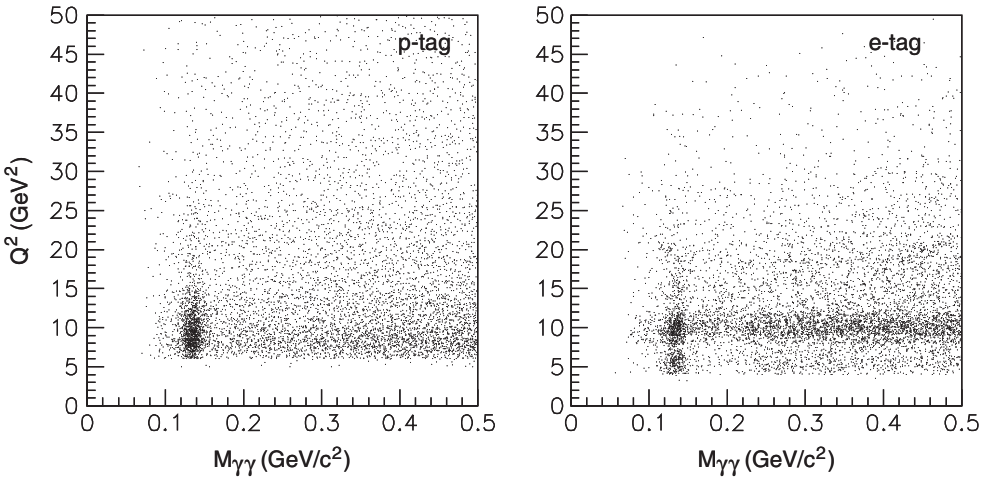

FIG. 11. Scatter plots of Q^2 versus $M_{\gamma\gamma}$ for the final experimental samples, shown separately for the p-tag (left) and e-tag (right) events.

systematic uncertainty induced by fixing these parameters is dominated by the large statistical error on the yield difference between the constrained and nonconstrained fits. We estimate this uncertainty by comparing the results obtained using two different sets of fit functions, as described in Sec. V E.

The following values for the fixed parameters were obtained from the MC: $m = 134$–137 MeV$/c^2$, $\sigma = 6$–9 MeV$/c^2$, $\Delta m = -5.5$–0.0 MeV$/c^2$, $1 - r = 0.11$–0.42 depending on Q^2 and the p- or e-tag; k is fixed at 2.4. The absolute values for these parameters tend to be larger when Q^2 is large. There are no significant anomalous tails in the signal $M_{\gamma\gamma}$ distribution down to the $\mathcal{O}(10^{-2})$ level of the peak, according to the signal MC, as shown in Fig. 12. Figure 13 shows the results of the fit to data in five representative Q^2 bins. The yields of the fits are summarized in Table I and are labeled $N_{\rm rec}$.

B. Estimation of background contamination

The measured π^0 yield could contain some contribution from background processes in which real π^0's are present in the final state. In this subsection, we explain how these resonant backgrounds are estimated and subtracted. First, possible backgrounds from e^+e^- annihilation processes are examined. A potentially large background from radiative-Bhabha events is also checked. Finally, we study the background contribution from the processes $\gamma\gamma^* \to \pi^0\pi^0$ and $e^+e^- \to (e)e\rho^0/\omega$, $\rho^0/\omega \to \pi^0\gamma$.

1. Backgrounds from e^+e^- annihilation processes

Backgrounds from e^+e^- annihilation are estimated by examining the yield of wrong-sign events, in which the tagged electron has the opposite sign to that expected in selection criterion (12). The electron charge in the final

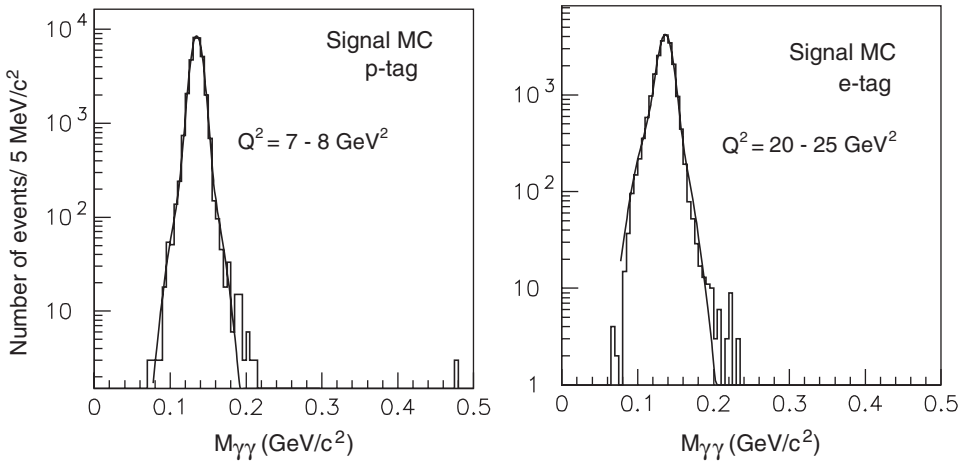

FIG. 12. $M_{\gamma\gamma}$ distributions for the signal MC events for the selected Q^2 ranges for the p-tag (left, 7 GeV$^2 < Q^2 <$ 8 GeV^2) and e-tag (right, 20 GeV$^2 < Q^2 <$ 25 GeV^2) samples. The curves are fits with a double-Gaussian function without background terms.

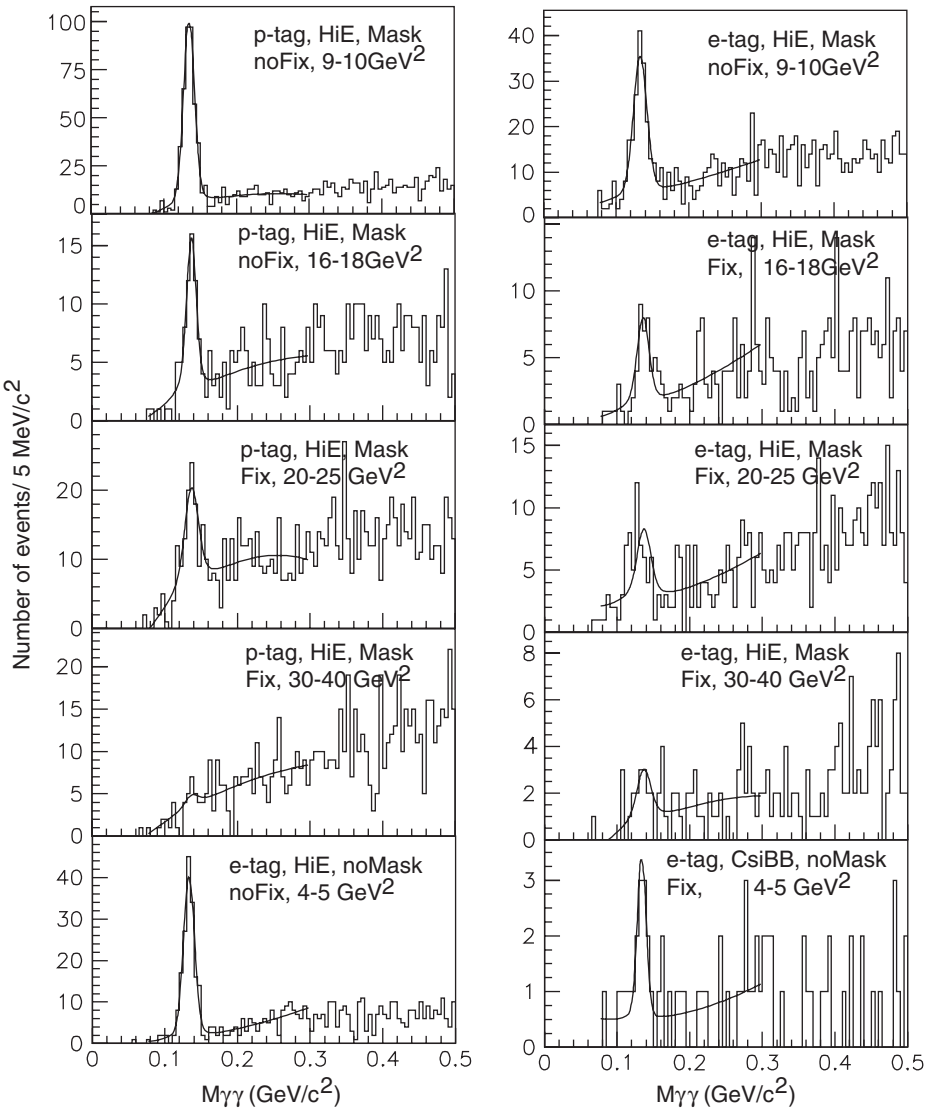

FIG. 13. Results of the fit to the experimental $M_{\gamma\gamma}$ distributions for representative Q^2 bins. The caption in each subfigure shows the type of tag (p- or e-tag), the required trigger, whether or not the Bhabha mask was applied (upper line), and whether or not the mass and resolution parameters (m and σ) are fixed in the fit and the Q^2 range (lower line).

state of the annihilation processes should have no significant forward-backward asymmetry. The contamination of this kind of background in the signal sample is expected to be the same as the number of events found in the wrong-sign samples.

We have studied the wrong-sign events by examining the parameter $E_{\rm ratio}$, whose distribution is shown in Fig. 14(a). We find that a small number of events peak near $E_{\rm ratio} = 1$ for the wrong-sign sample. However, there is no visible π^0 peak in the $M_{\gamma\gamma}$ distribution in any Q^2 regions as shown in Fig. 14(d). The yield in the π^0 peak is 1.2 ± 0.9 events in the sum of p- and e-tags with $Q^2 < 40$ GeV^2 for the total sample. We conclude that the neutral pions from e^+e^- annihilation processes do not contaminate the signal region $E_{\rm ratio} \simeq 1$, and the main background near $E_{\rm ratio} = 1$ is from the QED process $e^+e^- \to e^+e^-\gamma\gamma$, which is of order α^4. Although this process has a charge asymmetry, this is not a problem for background estimation since it does not peak at the pion mass.

We also conclude that any hadron or muon misidentified as a tagged electron is not accompanied by neutral pions and does not contribute to the peaking backgrounds. Hadrons or muons would appear with the same probability in the wrong-sign sample if they were significant in the right-sign signal sample. As seen in Figs. 14(b) and 14(c), the tail of the $E_{\rm ratio}$ distribution near the lower selection boundary (0.85) is dominated by the ISR tail of the signal process, which is accounted for in the signal MC down to $r_k = 0.25$. Some contributions from the peaking backgrounds ($(e)e\pi^0X$) discussed in Secs. IV B 3 and IV B 4 will also be present.

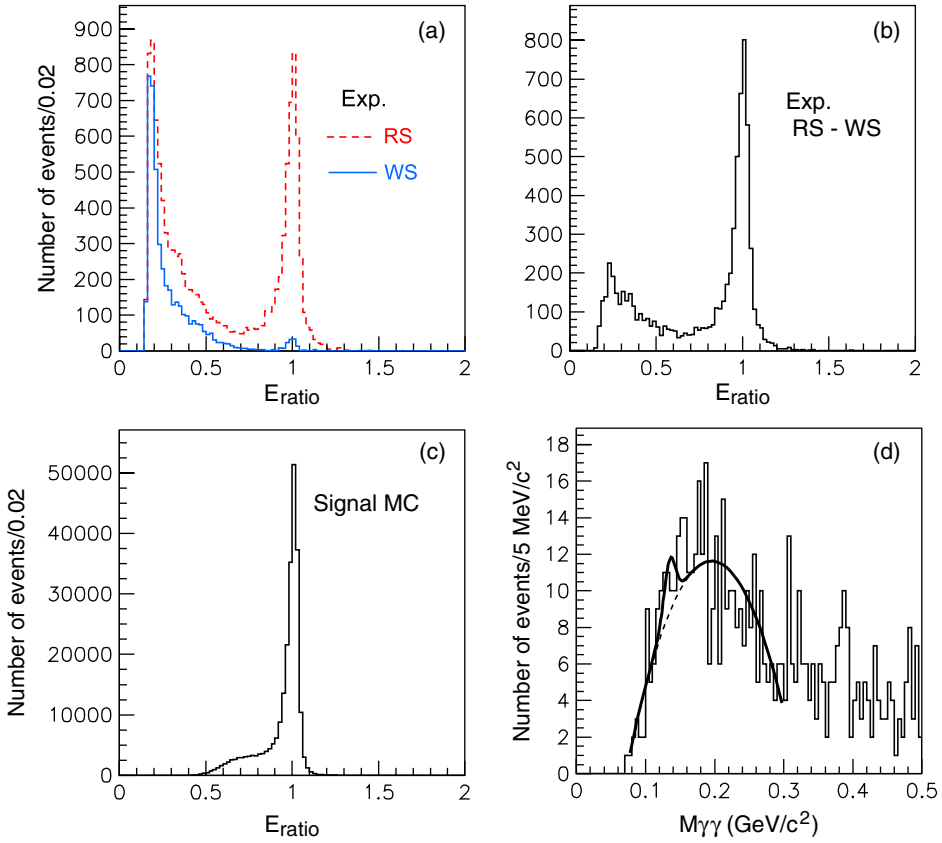

FIG. 14 (color online). (a) The E_{ratio} distribution for signal candidates for right-sign (RS, dashed line) and wrong-sign (WS, solid line) events. (b) The difference between RS events and WS events. (c) The E_{ratio} distribution for the signal MC sample. (d) The $M_{\gamma\gamma}$ distribution of wrong-sign events with the best fit superimposed (solid line) where the π^0 peak and the background contribution (dashed line) are taken into account in the fit.

2. Radiative-Bhabha backgrounds

Estimation of the radiative-Bhabha backgrounds where the photon is misreconstructed as a neutral pion is challenging. While the probability of such misreconstruction is small, the cross section of this background process is much greater than that of the signal process. A misidentification rate as small as $\mathcal{O}(10^{-6})$ can lead to background contamination. However, as described below, even in a conservative estimate, the background is negligibly small, safely less than one event in each high Q^2 bin.

The photon conversion process, $\gamma \to e^+e^-$, is the main source of radiative-Bhabha background, but almost all such events are rejected by selection criterion (11). Moreover, conversions can only give a broad distribution in $M_{\gamma\gamma}$. We estimate the background level to be negligibly small for $Q^2 < 20$ GeV^2 by extrapolating the $E_{\gamma\gamma}\Delta\theta$ distribution. Figure 15 shows this distribution for the experimental data and for signal and background MC, where the background contribution falls exponentially while the signal has a nearly flat distribution.

To check for additional background arising from radiative-Bhabha events, we study the possibility that some pions from a secondary interaction or beam background overlap with a radiative-Bhabha event where a photon escapes detection [$e^+e^- \to (e)e(\gamma) + \pi^0$(overlap)]. Note that there can be a solution satisfying the required three-body signal kinematics even if the photon is emitted at a forward angle. However, in this case, the background would have a broad E_{ratio} distribution concentrated at zero because the secondary π^0's are dominantly of low energy. There is a depletion of events around 0.8 in the E_{ratio} distribution as shown, e.g., in Fig. 14(a), even for the high Q^2 regions; we conclude that the contribution from this type of background is negligible.

There is a small probability that a photon from a radiative Bhabha converts to a neutral pion at the beam pipe or the central part of the detector, where the material thickness is kept to a minimum, via a soft nuclear interaction $\gamma A \to \pi^0 A'$. The pion is produced at forward angles with a small momentum transfer; the nucleus A can break up with an energy slightly larger than the binding energy. This cross section is poorly known, but we estimate that it is smaller than that for the elementary process $\gamma p \to \pi^0 p$ per nucleon. According to the previous measurements [22], the cross section for scattering angles below 10° is about 0.04 μb for incident photon energies between 2 and

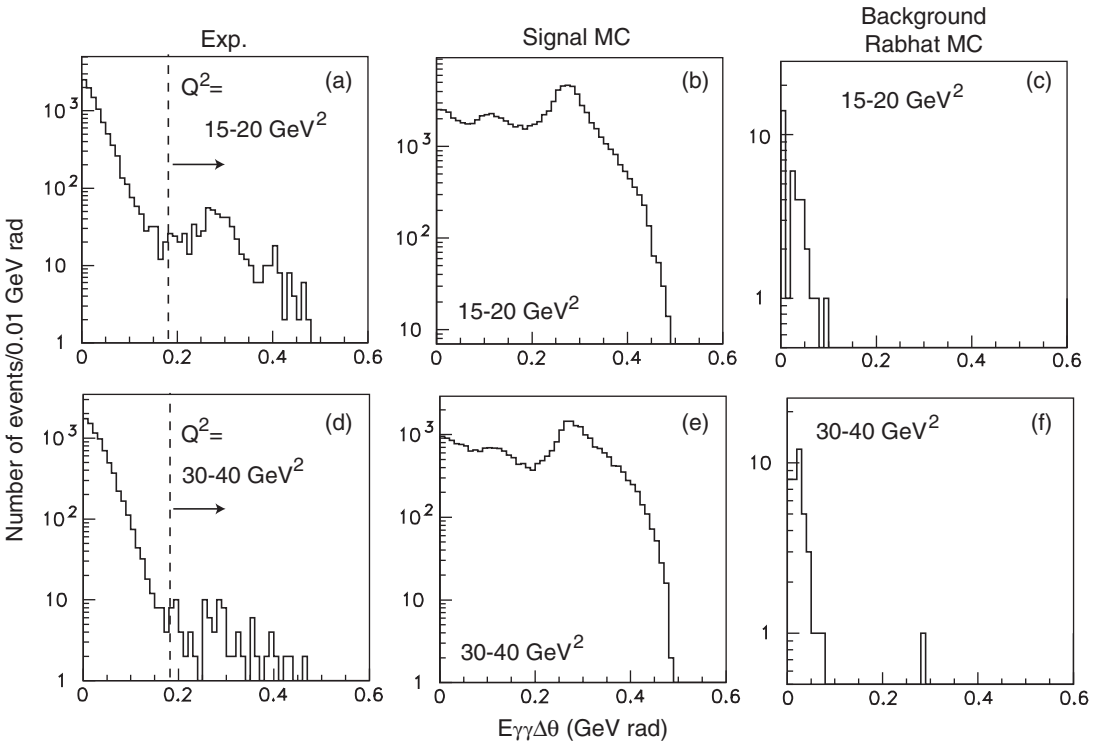

FIG. 15. The $E_{\gamma\gamma}\Delta\theta$ distributions for the (a), (d) experimental, (b), (e) signal MC, and (c), (f) radiative-Bhabha background MC samples, for two different Q^2 regions indicated in each subfigure. The dashed line shows the selection boundary. Arrows show the accepted regions. The background MC sample corresponds to an integrated luminosity 140 times smaller than the experimental data.

9 GeV. This cross section corresponds to a probability of 1.0×10^{-7} for a photo-nuclear conversion to a neutral pion with a similar energy. From the observed number of radiative-Bhabha events, we estimate that the contamination is at most a 0.5 event in the highest Q^2 bin and negligible for all other bins. We thus conclude that the background from this source in all Q^2 bins is small, and assign 3% and 1% uncertainties only to the two highest Q^2 bins.

3. Background from $\gamma\gamma^* \to \pi^0\pi^0$

Processes with one extra particle, i.e., $e^+e^- \to (e)e\pi^0 X$, where X is another π^0 or photon, could also be a source of resonant background that would have to be subtracted from the measured π^0 yield in each bin of Q^2.

This type of background may have both a charge asymmetry that favors the right sign and a peak at the π^0 mass. For large X invariant masses, this background is suppressed by the $E_{\rm ratio}$ selection criterion. However, if the invariant mass and the momentum of X are small, $E_{\rm ratio}$ approaches unity, and we cannot use it to distinguish between signal and background processes.

To study such background, we use a rather loose set of selection criteria to positively identify $e^+e^- \to (e)e\pi^0\pi^0$ candidates that contribute in a wide kinematical range. There should be four or more photons in the final state; we accept the extra pion with a loose energy constraint. We apply a selection requirement on the energy of the $\pi^0\pi^0$ system using an energy ratio similar to $E_{\rm ratio}$ to enhance three-body kinematical configurations. We take the ratio of the observed energy to the expected energy calculated using the observed invariant mass for the $\pi^0\pi^0$ system.

An MC generator was developed for this background process with an equivalent photon approximation to reproduce the $W(\equiv M_{\pi\pi})$ and c.m.-scattering-angle distributions. We assume that the angular distribution is the same as that in the no-tag process [23], inspired by the observed distribution. The W distribution is tuned to the experimental data. Figure 16 shows the experimental data and the background MC in a two-dimensional plot of the $\pi^0\pi^0$ invariant mass and cosine of the scattering angle (θ^*) of the π^0 in the $\pi^0\pi^0$ rest frame with respect to the $\gamma\gamma^*$ collision axis. The Q^2 dependence of the cross section is tuned to reproduce the data before determining the background contribution for each Q^2 bin. We normalize the background size to the observed background yield. We find that events from the signal process, $(e)e\pi^0$ with misidentified photons, produce a background in the sample of $(e)e\pi^0\pi^0$ at extremely forward or backward scattering angles near an invariant mass of 1 GeV/c^2. We subtract this component in the evaluation of the background. In total, 1305 events are found for the process $e^+e^- \to (e)e\pi^0\pi^0$ with $|\cos\theta^*| < 0.9$.

Using $e^+e^- \to (e)e\pi^0\pi^0$ MC, the background contribution from this process is estimated to be about 2% of the signal yield, with a negligible Q^2 dependence. This is

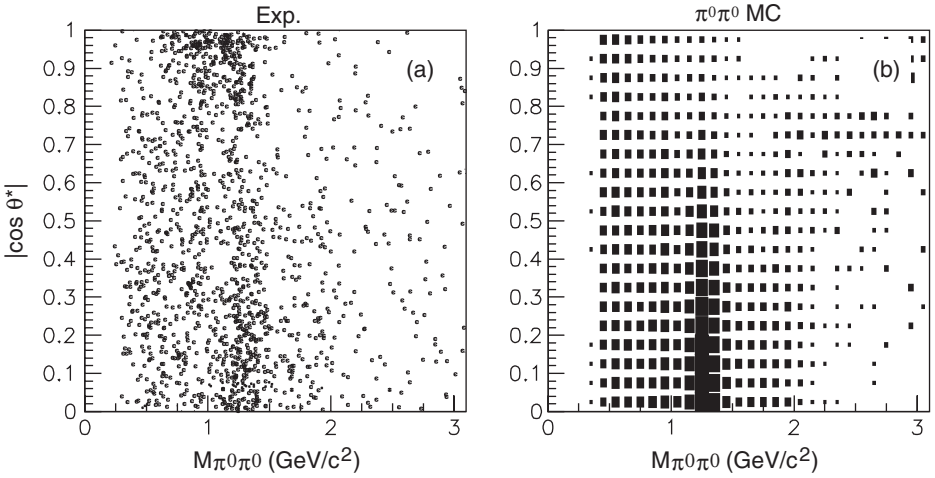

FIG. 16. Two-dimensional plots of $|\cos\theta^*|$ versus invariant mass of the $\pi^0\pi^0$ system for the selected $(e)e\pi^0\pi^0$ events (a) for the experimental data and (b) for the $(e)e\pi^0\pi^0$ MC samples.

accounted for as a background factor in the calculation of the cross section for the signal process.

4. Background from $e^+e^- \to (e)e\rho^0/\omega$, $\rho^0/\omega \to \pi^0\gamma$

A similar background from $e^+e^- \to (e)e\rho^0/\omega$, $\rho^0/\omega \to \pi^0\gamma$ is also studied. This process can contribute to background through a virtual pseudo-Compton process, where the final-state photon is replaced by a neutral vector meson. We have searched for events that could be described by this process by requiring an extra detected photon with a loose energy constraint. We find about 180 events with the $\pi^0\gamma$ invariant mass peaking at the nominal ω mass. Figure 17 shows the experimental data in a two-dimensional plot of the $\pi^0\gamma$ invariant mass versus the cosine of the scattering angle (θ^*) of the π^0 in the $\pi^0\gamma$ rest frame with respect to the $\pi^0\gamma$ momentum direction. Events with an ω dominate, although it is difficult to separate them from a possible ρ^0 contribution. In Fig. 17, the horizontal band seen at $|\cos\theta^*| > 0.9$ is from the signal process $[e^+e^- \to (e)e\pi^0]$ with a misidentified photon. This contribution is removed when we estimate the $\rho^0/\omega \to \pi^0\gamma$ background.

We simulate this background in MC by replacing the $e\gamma$ system in Rabhat by an $e\omega$ system with the same invariant mass and let them scatter at the same angle in the $e\gamma$ (thus, $e\omega$) rest frame. We normalize the MC sample to the observed number of background events and estimate the background to the signal process. The result is Q^2 dependent because the background process is not a two-photon process; it varies from 0.8% for the low Q^2 bin to 3% for the highest Q^2 bin. This is accounted for as a background factor in the derivation of the cross section for the signal process.

The background yield can be estimated by a generalized vector-meson dominance model (GVDM) factor in which a photon is replaced by a neutral vector-meson, with branching fractions for $\rho^0/\omega \to \pi^0\gamma$ decays. The GVDM factors for the ρ^0 and ω are assumed to be $1/300$ and $1/3000$, respectively [24]. Multiplying them by the branching fractions to $\gamma\pi^0$, we obtain a factor of $1/32\,000$ for the probability of the background process compared to the VC process. With the estimated efficiency of 1.5×10^{-4} from the background MC, the expected background yield from the GVDM is 120 events. This estimate is within a factor of 2 of the observed background.

We conclude that the backgrounds discussed in Secs. IV B 1 and IV B 2 are negligible. The total contribution from the backgrounds described in IV B 3 and IV B 4 is shown in column 6 of Table I.

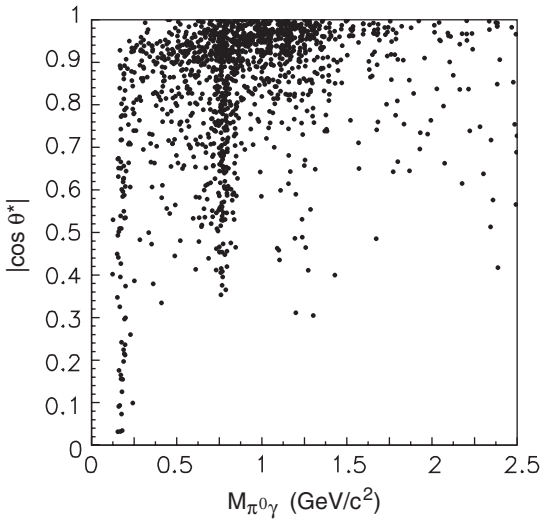

FIG. 17. Scatter plot for the selected $(e)e\pi^0\gamma$ events: $|\cos\theta^*|$ versus invariant mass of the $\pi^0\gamma$ (see the text for the definition of the θ^*).

V. MEASUREMENT OF DIFFERENTIAL CROSS SECTION AND TRANSITION FORM FACTOR

In this section, we first describe the method of Q^2 unfolding and the determination of the representative Q^2 value for each Q^2 bin. We then outline how the cross section is measured. This is followed by the evaluation of the systematic uncertainties and some cross-checks. The transition form factor for π^0 is then determined. Finally, the observed TFF is compared with previous experiments and empirical parametrizations.

A. Procedure for Q^2 unfolding

The π^0 yield is measured in bins of reconstructed momentum transfer $Q^2_{\rm rec}$. We approximate the true value of Q^2 with the corrected value $Q^2_{\rm cor}$. We use signal MC events to calculate the folding matrix A_{ij} for a total of 15 bins in Q^2, of 1 GeV^2 width for 5–12 GeV^2, 2 GeV^2 width for 12–20 GeV^2, 5 GeV^2 width for 20–30 GeV^2, and 10 GeV^2 width for 30–50 GeV^2. This is done separately for the p- and e-tags. In our algorithm, we include bins that are not used to calculate the TFF. The generated events are weighted to have a realistic Q^2 dependence $d\sigma/dQ^2 \propto Q^{-7}$, which is consistent with the data.

The number of events in the same bin before and after the unfolding is expressed by

$$n_{i,\rm rec} = \sum_j A_{ij} n_{j,\rm cor}, \tag{17}$$

where $n_{i,\rm rec}$ is the number of events in the ith bin before the unfolding, which is based on the measured Q^2, and $n_{j,\rm cor}$ is the number of events in the jth bin after the unfolding, which is based on the true Q^2. By definition, $\sum_i A_{ij}$ is normalized to unity. A_{ij} is close to a unit matrix, and the majority of the off-diagonal elements are close to zero except for the components adjacent to the diagonal. We calculate the inverse matrix, which is also close to diagonal. The edge bins in the inverse matrix are irregular because no experimental measurements are available. To avoid bias, we do not derive $n_{j,\rm cor}$ near the edge bins, and use the unfolding method described above to obtain results only for the range 7–30 GeV^2.

For the other bins near the edge, we correct the measurement by the factor $f_i = \sum_j N_{ji}/\sum_j N_{ij}$, where N_{ij} is the unnormalized original matrix obtained from the Q^{-7}-dependent MC simulation; this method yields correct results when MC events are generated with a realistic Q^2 dependence. Figure 18 shows the number of events in each bin before and after the unfolding. The effect of the unfolding is small, but the statistical uncertainty increases slightly. The resulted numbers after the unfolding are tabulated as $N_{\rm cor}$ in Table I.

B. Representative $\bar{Q}^2$ values for each bin

We define the representative Q^2 for each bin with a finite bin width, $\bar{Q}^2$, using the formula

$$\frac{d\sigma}{dQ^2}(\bar{Q}^2) = \frac{1}{\Delta Q^2}\int_{\rm bin}\frac{d\sigma}{dQ^2}(Q^2)dQ^2, \tag{18}$$

where ΔQ^2 is the bin width. We assume an approximate dependence of $d\sigma/dQ^2 \propto Q^{-7}$ for the calculation. The representative values are shown in the leftmost column of Table I.

C. Extraction of differential cross section

The number of signal events is obtained by the fit procedure shown in Sec. IV A in each Q^2 bin, separately for the e-tag and p-tag samples. To take into account event migration among bins due to finite resolution, the number of events observed in each Q^2 bin is corrected using the unfolding method described in Sec. V A. The number of events is then converted to the cross section for $e^+e^- \to (e)e\pi^0$ using the following formula:

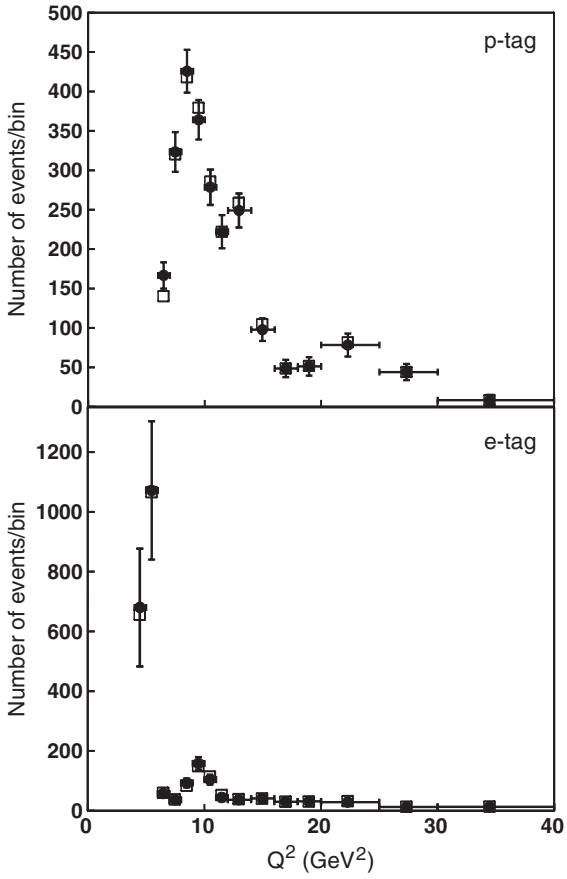

FIG. 18. The number of events for the signal candidates in Q^2 bins before and after the unfolding. Note that the yield is not normalized to the bin width, and the background yield is not subtracted. The open squares (dots with error bars) are the yields before (after) the Q^2 unfolding. The vertical error bars are statistical and are only shown for the plots after the unfolding. The data points at $Q^2 < 6$ GeV^2 for the e-tag are the results from the HiE + 50 * CsiBB sample.

$$\frac{d\sigma}{dQ^2} = \frac{N(1-b)}{\eta\mathcal{B}\int\mathcal{L}dt(1+\delta)\Delta Q^2}, \tag{19}$$

where N is the number of signal events in the bin, b is the fraction of the estimated π^0 peaking background in the yield, and η is the efficiency corrected for the beam energy difference between the $\Upsilon(4S)$ and $\Upsilon(5S)$, which is the mean of the efficiencies weighted by the ratio of the integrated luminosities and the $2A(Q^2)$ parameter for different beam energies. Using this procedure, the differential cross section is obtained at the e^+e^- c.m. energy of the $\Upsilon(4S)$. Here, $\mathcal{B}$ is the branching fraction for $\pi^0 \to \gamma\gamma$, $\int\mathcal{L}dt$ is the total integrated luminosity, and $1+\delta$ is the radiative correction for $r_k^{\max} = 0.25$ used to determine the cross section for the tree-level diagrams. The value of δ is -1% or $+2\%$ without or with a correction for hadronic vacuum polarization [25], respectively; we adopt the latter value. We include its Q^2 dependence, which is around 1% in the kinematical region of the present measurement, into the systematics. The quantity ΔQ^2 is the bin width in Q^2.

We extract the cross section of $e^+e^- \to (e)e\pi^0$ defined in the range $Q_2^2 < 1$ GeV^2, where Q_2^2 is the Q^2 of the photon with smaller virtuality. Our measurement is performed in a small Q_2^2 region, mainly less than 0.01 GeV^2, and then the upper bound is extrapolated to 1.0 GeV^2. The requirement for the incident photon with the smaller virtuality (which is the Q^2 requirement in this paper) depends on the experiment and hence the definition of the cross section is somewhat dependent on the experiment. The result of this procedure is shown in Fig. 19. The differential cross sections are shown separately for the p- and e-tags in Table II.

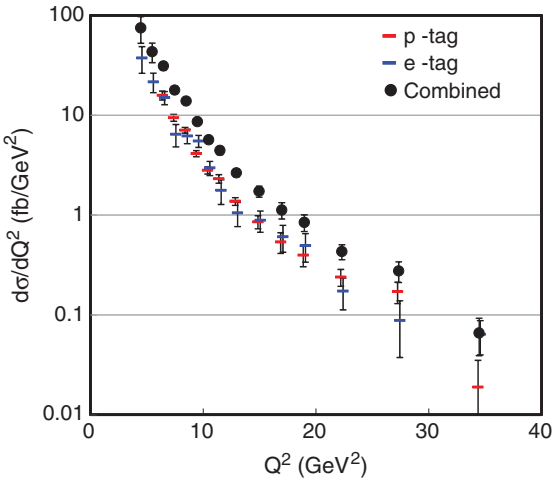

FIG. 19 (color). Results for the $e^+e^- \to (e)e\pi^0$ differential cross section. "Combined" corresponds to twice the weighted average of the p-tag and e-tag results. Error bars show statistical uncertainties only. The horizontal positions in the p-tag and e-tag plots are shifted slightly relative to each other to make it easier to see the sizes of the statistical uncertainties.

We find that the differential cross sections are consistent between the p- and e-tag measurements. The difference between the two measurements in the same Q^2 region is smaller than 1.8σ, where σ is the combined statistical error, for each Q^2 bin as shown in Fig. 20. We combine the p- and e-tag results for the same Q^2 bin, if available, by taking the weighted average of the results with a weight that is the inverse square of the statistical error. We then double the average. Where only the result from the e-tag is available (for the Q^2 range of 4–6 GeV^2), we simply double the value. The differential cross sections combined for the p- and e-tags are shown in Table III.

The obtained differential cross sections are compared with those from the previous experiments [1,4] in Fig. 21. Although the definitions of the differential cross sections differ slightly between the experiments, the difference should be compensated in the algorithms used to extract the transition form factor. Later in this section, we compare in more detail the π^0-TFF results obtained by different experiments.

D. Determination of the transition form factor

The $e^+e^- \to (e)e\pi^0$ cross section is converted to the transition form factor squared by dividing it by $2A(\bar{Q}^2)$. Finally, we obtain

$$Q^2|F(Q^2)| = Q^2\sqrt{\frac{d\sigma/dQ^2(Q^2)}{2A(Q^2)}}, \tag{20}$$

where Q^2 replaces the symbol $\bar{Q}^2$. The results for this product are shown in Fig. 22 and Table III.

E. Systematic uncertainties and some checks

The estimates of systematic uncertainties for the Q^2 differential cross sections are described in this subsection. They can be divided into Q^2-dependent and -independent contributions.

1. Estimates of systematic uncertainties

The Q^2-independent contributions in the systematic uncertainty include tracking uncertainty (1%), electron-ID (1%), $\gamma\gamma$-pair reconstruction efficiency (3%), kinematical selection (2%), geometrical selection including the trigger (2%), beam-background effects that affect the event reconstruction (2%), and integrated luminosity (1.4%). These are correlated Q^2-independent uncertainties, resulting in a total of 5% in the quadratic sum for the systematic uncertainty arising from the efficiency. Note that we do not use a conventional π^0 reconstruction from a mass-constrained fit, as we fit experimental $\gamma\gamma$ mass spectra. The peaking-background contamination (1%–4%), fit error in the π^0-yield extraction (5%–10%), and the trigger efficiency (2%–12%) have significant Q^2 dependence. We estimate the fit uncertainty by taking the difference between the central values and a simpler fit with a single Gaussian and a

TABLE II. $e^+e^- \to (e)e\pi^0$ differential cross section and systematic uncertainties in bins of Q^2 summarized for the p- and e-tags separately. The "Q^2-independent syserr" and "Q^2-dependent efficiency syserr" uncertainties are described in Sec. V E.

Tag	Q^2 (GeV^2)	$d\sigma/dQ^2$ (fb/GeV^2)	Q^2-independent syserr (%)	Q^2-dependent efficiency syserr (%)	Fit syserr (%)	Peaking-bkg syserr (%)	Total syserr (%)
	6.47	15.85 ± 1.63	6	4	4	2	8
	7.47	9.47 ± 0.76	6	2	4	2	8
	8.48	7.09 ± 0.47	6	2	4	2	8
	9.48	4.13 ± 0.29	6	2	4	2	8
	10.48	2.81 ± 0.23	6	2	4	2	8
	11.48	2.31 ± 0.23	6	3	4	2	8
p	12.94	1.37 ± 0.12	6	10	4	2	12
	14.95	0.857 ± 0.129	6	12	4	2	14
	16.96	0.539 ± 0.127	6	10	4	2	12
	18.96	0.397 ± 0.093	6	10	4	2	12
	22.29	0.240 ± 0.046	6	5	10	2	13
	27.33	0.172 ± 0.042	6	5	10	2	13
	34.46	0.019 ± 0.016	6	5	10	4	13
	4.46	37.5 ± 11.2	6	2	7	2	10
	5.47	21.6 ± 4.8	6	1	7	2	9
	6.47	15.03 ± 2.26	6	8	7	2	12
	7.47	6.45 ± 1.63	6	5	7	2	11
	8.48	6.21 ± 1.02	6	5	7	2	11
	9.48	5.53 ± 0.76	6	5	7	2	11
	10.48	2.97 ± 0.48	6	5	7	2	11
e	11.48	1.77 ± 0.49	6	5	7	2	11
	12.94	1.05 ± 0.29	6	8	7	2	12
	14.95	0.886 ± 0.213	6	10	7	2	14
	16.96	0.607 ± 0.183	6	10	7	2	14
	18.96	0.495 ± 0.157	6	10	7	2	14
	22.29	0.173 ± 0.061	6	10	10	2	15
	27.33	0.088 ± 0.051	6	10	10	2	15
	34.46	0.064 ± 0.024	6	10	10	4	16

linear background applied for the narrower $M_{\gamma\gamma}$ fit range, 0.08–0.20 GeV/c^2. We evaluate the systematic uncertainty due to this $M_{\gamma\gamma}$ fitting by averaging the deviations in the fit results in each of two Q^2 regions (below and above $Q^2 = 20$ GeV^2) for each of the p- and e-tags to compensate for the statistical fluctuations, as listed in column 6 of Table II.

To estimate the systematic uncertainty in the trigger efficiency, we study the efficiency using a radiative-Bhabha process; we find agreement between the data and the Rabhat MC at the 5%–10% level, as shown in Figs. 30(c) and 30(d) (Appendix B 3). In addition, the comparison of the absolute yields of the radiative-Bhabha events shows consistency between the data and MC also within 10% level, which is comparable to the estimated size of systematic uncertainty without including the uncertainty from the trigger efficiency of ~8% [see Figs. 29(c) and 29(d) and the text in Appendix B 3]. Therefore, we conclude that the systematic uncertainty in the trigger efficiency does not exceed the deviations seen in studies using radiative-Bhabha events: 12% for the p-tag and 10% for the e-tag, where the values are taken from the overall tendency of the deviations in the Q^2 dependence shown in Figs. 29(c), 29(d), 30(c), and 30(d). However, we do expect the systematic uncertainty to be smaller for many individual Q^2 bins, e.g., in bins where the effect of the Bhabha-veto threshold is relatively small and the trigger efficiency is not very sensitive to it. To obtain the Q^2-dependent systematic error, we have varied the Bhabha-veto trigger threshold by ±0.2 GeV in the trigger simulation applied to the signal MC events and taken the change of the efficiency for each bin if it is smaller than the maximum values mentioned above. In practice, we have found that the variation has a large Q^2 dependence, ranging from 2% to 25%, in each of the p- and e-tag samples. We replace the uncertainty determined by the variation of the trigger threshold in the signal MC by 12% (10%) for the p-tag (e-tag) case if the former is greater than 12% (10%) in an individual Q^2 bin. We replace the systematic uncertainty in the bin $Q^2 = 14$–16 GeV^2 for the p-tag sample and in the six bins in the Q^2 range 14–40 GeV^2 for the e-tag sample.

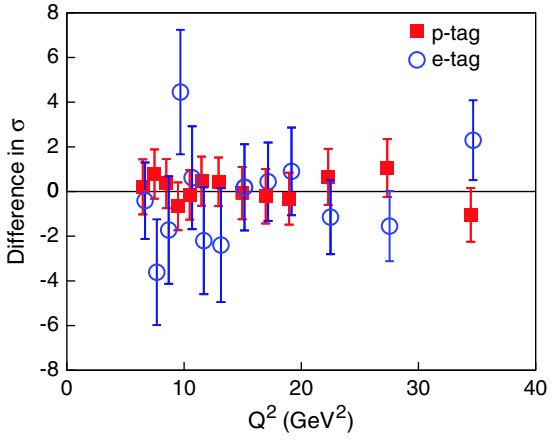

FIG. 20 (color online). Differences between the $e^+e^- \to (e)e\pi^0$ differential cross section measured by the p-tag (squares) and e-tag (circles) from their weighted mean (equal to a half of the combined cross section). The vertical scale is normalized by the error of the weighted mean (which is the same as half of the error for the combined cross section). The horizontal positions of the p-tag and e-tag plots are displaced intentionally so that the error bars are visible.

We assign a $\pm(1\%$–$3\%)$ systematic uncertainty from a possible deviation of the Q^2 dependence in the signal MC from the data distribution for the lowest two bin results in each of the p- and e-tags. In other Q^2 regions, this uncertainty is negligibly small. We take the difference between the calculated efficiencies with two assumed Q^2 dependences: $|F(Q^2)|^2 \sim 1$ and $|F(Q^2)|^2 \sim 1/Q^2$. The combined uncertainties from this source and from the trigger efficiency are shown in Table II as a Q^2-dependent systematic uncertainty in the efficiency. The evaluation of uncertainties is performed separately for the p- and e-tags.

In addition, the uncertainties from the calculation of the radiative corrections (3%) and assumed form factor effects for the photon with smaller virtuality (1.0%) enter when determining the differential cross section. The correlated Q^2-independent uncertainty is in total 6%, of which 5% is from the efficiency determination as described above, in a quadrature sum for the uncertainty in the differential cross section.

TABLE III. $e^+e^- \to (e)e\pi^0$ differential cross section combined for the p- and e-tags with systematic uncertainties ($\epsilon_{\rm sys}$) and the transition form factor $Q^2|F(Q^2)|$. The first and second uncertainties for $Q^2|F(Q^2)|$ are statistical and systematic, respectively.

Q^2 (GeV^2)	$d\sigma/dQ^2$ (fb/GeV^2)	$\epsilon_{\rm sys}$ (%)	$Q^2\lvert F(Q^2)\rvert$ (GeV)
4.46	75.0 ± 22.3	10	$0.129 \pm 0.020 \pm 0.006$
5.47	43.3 ± 9.6	9	$0.140 \pm 0.016 \pm 0.007$
6.47	31.15 ± 2.64	10	$0.161 \pm 0.007 \pm 0.008$
7.47	17.86 ± 1.38	8	$0.158 \pm 0.006 \pm 0.007$
8.48	13.88 ± 0.85	8	$0.175 \pm 0.005 \pm 0.007$
9.48	8.62 ± 0.55	8	$0.169 \pm 0.005 \pm 0.007$
10.48	5.68 ± 0.42	8	$0.165 \pm 0.006 \pm 0.007$
11.48	4.44 ± 0.41	9	$0.173 \pm 0.008 \pm 0.007$
12.94	2.65 ± 0.23	12	$0.168 \pm 0.007 \pm 0.010$
14.95	1.73 ± 0.22	14	$0.179 \pm 0.012 \pm 0.013$
16.96	1.123 ± 0.208	13	$0.183 \pm 0.017 \pm 0.012$
18.96	0.845 ± 0.160	13	$0.198 \pm 0.019 \pm 0.013$
22.29	0.431 ± 0.074	14	$0.195 \pm 0.017 \pm 0.013$
27.33	0.275 ± 0.064	14	$0.236^{+0.026}_{-0.029} \pm 0.016$
34.46	0.066 ± 0.027	14	$0.188^{+0.035}_{-0.043} \pm 0.013$

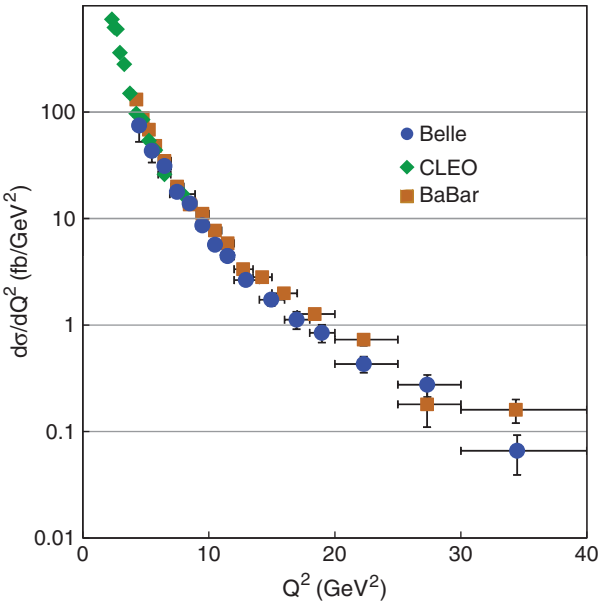

FIG. 21 (color). Comparison of the results for the $e^+e^- \to (e)e\pi^0$ differential cross sections among different experiments. The vertical error bars are statistical only. The algorithms used to measure the cross section differ between the experiments.

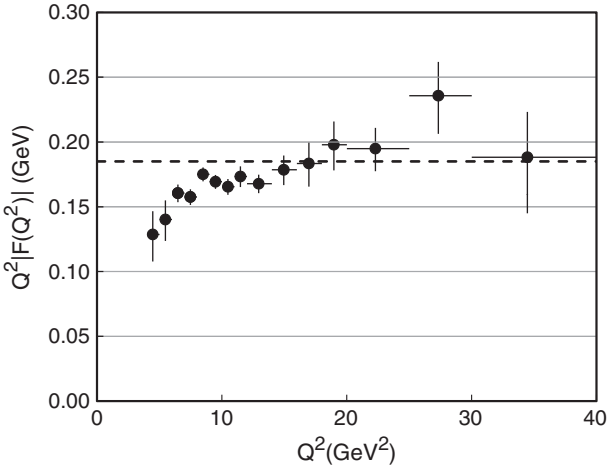

FIG. 22. Results for the π^0 transition form factor from the present measurement multiplied by Q^2. The error bars are statistical only. The dashed line shows the asymptotic limit from pQCD (~ 0.185 GeV).

The total systematic uncertainties for the combined differential cross section and for the transition form factor are shown in Tables II and III. We assume that the systematic uncertainties in the p- and e-tags correlate maximally. Because the transition form factor is derived from the square root of the cross section, the relative systematic uncertainty is half of the above. The calculation uncertainty for the conversion factor $2A(Q^2)$, 2%, is small compared to other sources of uncertainties. The uncertainty in the value of $\bar{Q}^2$ in each bin is also negligible ($\Delta\bar{Q}^2/\bar{Q}^2 \sim 0.3\%$) because $Q^2|F(Q^2)|$ varies slowly with Q^2.

2. Check for ISR in the signal process

We have included the effect of ISR in the signal MC simulation but only for the tagged electron side with exponentiation. This is a reasonable approximation because only the tag-side shifts Q^2 and kinematics significantly, while low-Q^2 radiation from the untagged side does not change any observable. The corrections in δ are small for both cases (at the 2% level). We compare the r_k distributions in data after background subtraction using the π^0-mass sideband events and the signal MC samples after the selection as shown in Fig. 23. The fraction of energy from radiation relative to the beam energy, r_k [defined in Eq. (14)], is calculated by an approximate kinematical relation from the observed variables,

$$r_k = \frac{\sqrt{s} - (E^*_\pi + E^*_e) - |\boldsymbol{p}^*_\pi + \boldsymbol{p}^*_e|}{\sqrt{s}}. \qquad (21)$$

In the *BaBar* analysis, this parameter is directly used as a selection [1]. In our analysis, instead of r_k we use the variable $E_{\rm ratio}$. These two variables are strongly correlated, as, kinematically, $E_{\rm ratio} = 1$ when $r_k = 0$. The peak and the core part of the r_k distribution ($-0.02 < r_k < 0.06$) are safely contained by our selection criteria for $E_{\rm ratio}$, so the consistency between the data and MC after this selection permits a reliable determination of the signal efficiency. As the signal MC events are generated with $r_k^{\rm max} = 0.25$, no bias is introduced in the signal region by our selection criteria.

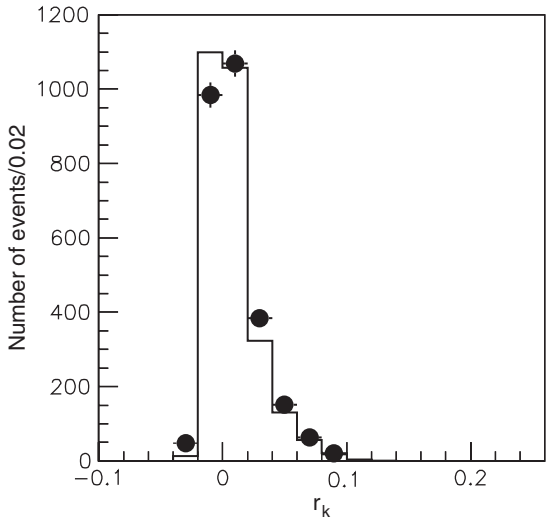

FIG. 23. Distribution of the ISR energy fraction (r_k) calculated from observables in data (solid dots) and in the signal MC samples (histogram). The data distribution is shown after background subtraction. The MC events are normalized to the experimental yield after background subtraction. Note that there are uncertainties in the value of r_k originating from the measurement and kinematical approximation.

F. Comparison with previous measurements and empirical fits

The measured product $Q^2|F(Q^2)|$ is compared with the previous measurements [1,3,4] in Fig. 24. Our results agree with previous measurements within uncertainties for Q^2 below 9 GeV^2; in the higher Q^2 region, they do not show the rapid growth observed by *BaBar* [1].

BaBar has suggested a parametrization fit with the functional form

$$Q^2|F(Q^2)| = A\left(\frac{Q^2}{10\text{GeV}^2}\right)^\beta, \qquad (22)$$

where A and β are fit parameters. *BaBar* reported $A = 0.182 \pm 0.002$ GeV and $\beta = 0.25 \pm 0.02$; however, the uncertainty for A does not include the Q^2-independent systematic uncertainty that amounts to 2.3% [namely ± 0.0041 GeV as this error component for $Q^2|F(Q^2)|$]. Taking this into account, the uncertainty on A reported by *BaBar* could be replaced by $A = 0.182 \pm 0.005$ GeV.

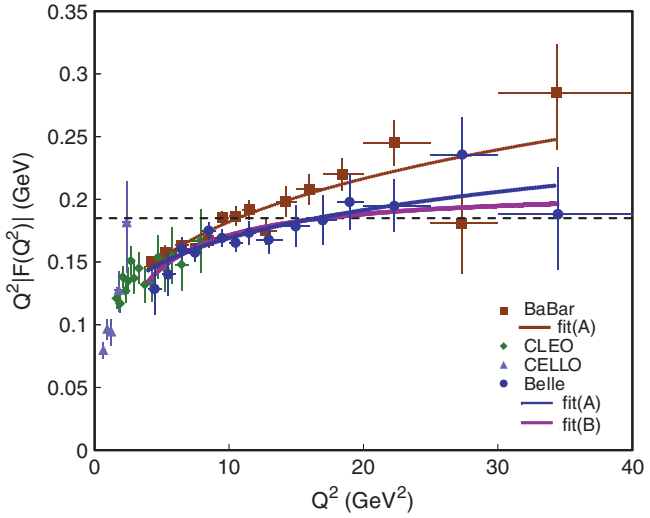

FIG. 24 (color). Comparison of the results for the product $Q^2|F(Q^2)|$ for the π^0 from different experiments. The error bars are a quadratic sum of statistical and systematic uncertainties. For the Belle and *BaBar* results, only a Q^2-dependent systematic-error component is included. The two curves denoted fit(A) use the *BaBar* parametrization while the curve denoted fit (B) uses Eq. (23) (see the text). The dashed line shows the asymptotic prediction from pQCD (~ 0.185 GeV).

To compare our results with *BaBar*'s, we use the same parametrization in our fit procedure and assume a Q^2-independent systematic uncertainty (thus, the total normalization error) of 3.2% for $Q^2|F(Q^2)|$; we remove this component from the combined statistical and systematic errors and instead add it in quadrature to the uncertainty in A. The fit results from Belle are $A = 0.169 \pm 0.006$ GeV and $\beta = 0.18 \pm 0.05$. The goodness of the fit is $\chi^2/\mathrm{ndf} = 6.90/13$, where ndf is the number of degrees of freedom. The fit results are also shown in Fig. 24. The fit of the Belle data to the function is good, and we find a difference of $\sim 1.5\sigma$ between the Belle and *BaBar* results in both A and β.

We then try another parametrization in which $Q^2|F(Q^2)|$ approaches an asymptotic value, namely,

$$Q^2|F(Q^2)| = \frac{BQ^2}{Q^2 + C}. \tag{23}$$

The fit gives $B = 0.209 \pm 0.016$ GeV and $C = 2.2 \pm 0.8$ GeV^2 with $\chi^2/\mathrm{ndf} = 7.07/13$, and is also shown in Fig. 24. The fitted asymptotic value, B, is slightly larger than the pQCD value of ~ 0.185 GeV but is consistent.

For a simple estimate of the consistency between the Belle and *BaBar* results, we compare the data from individual experiments with a reference curve obtained by fitting the data from both experiments together using the parametrization of Eq. (23). The seven data points from Belle (from *BaBar*) for the range 9 GeV$^2 < Q^2 <$ 20 GeV^2, where the two measurements seem to be systematically shifted, deviate from the reference curve by $(-6.1 \pm 3.8)\%$ [by $(+4.8 \pm 3.0)\%$] in average relative to it. We incorporate the Q^2-independent uncertainty in each measurement in the above error. The difference between the Belle and *BaBar* deviations, $(10.9 \pm 4.8)\%$, corresponds to a 2.3σ significance. This result does not depend on choice of the reference curve.

VI. SUMMARY AND CONCLUSION

We have presented a measurement of the neutral pion transition form factor for the process $\gamma\gamma^* \to \pi^0$ in the region 4 GeV$^2 \lesssim Q^2 \lesssim 40$ GeV^2 with a 759 fb^{-1} data sample collected with the Belle detector at the KEKB asymmetric-energy e^+e^- collider. The measured values of $Q^2|F(Q^2)|$ agree with the previous measurements [1,3,4] for $Q^2 \lesssim 9$ GeV^2. In the higher Q^2 region, in contrast to *BaBar*, our results do not show a rapid growth with Q^2 and are closer to theoretical expectations [5].

ACKNOWLEDGMENTS

We are indebted to Drs. Y. Kurihara and K. Tobimatsu for their helpful suggestions in the tuning of the Rabhat and Bases/Spring programs to match our configuration. Valuable discussions with Dr. V. Chernyak are acknowledged. We are also grateful to the BabaYaga team for their efforts in developing and providing a modified version of BabaYaga suitable for radiative-Bhabha event generation for our kinematical configuration, although we could not make use of it properly. We thank the KEKB group for the excellent operation of the accelerator, the KEK cryogenics group for the efficient operation of the solenoid, and the KEK computer group and the National Institute of Informatics for valuable computing and SINET4 network support. We acknowledge support from the Ministry of Education, Culture, Sports, Science, and Technology (MEXT) of Japan, the Japan Society for the Promotion of Science (JSPS), and the Tau-Lepton Physics Research Center of Nagoya University; the Australian Research Council and the Australian Department of Industry, Innovation, Science, and Research; the National Natural Science Foundation of China under Contracts No. 10575109, No. 10775142, No. 10875115, and No. 10825524; the Ministry of Education, Youth and Sports of the Czech Republic under Contracts No. LA10033 and No. MSM0021620859; the Department of Science and Technology of India; the BK21 and WCU program of the Ministry Education Science and Technology, National Research Foundation of Korea, and NSDC of the Korea Institute of Science and Technology Information; the Polish Ministry of Science and Higher Education; the Ministry of Education and Science of the Russian Federation and the Russian Federal Agency for Atomic Energy; the Slovenian Research Agency; the Swiss National Science Foundation; the National Science Council and the Ministry of Education of Taiwan; and the U.S. Department of Energy and the National Science Foundation. This work is supported by a Grant-in-Aid from MEXT for Science Research in a Priority Area ("New Development of Flavor Physics"), and from JSPS for Creative Scientific Research ("Evolution of Tau-lepton Physics").

APPENDIX A: BHABHA-VETO AND BHABHA-MASK SELECTION

The Bhabha veto in the HiE trigger of the Belle trigger system rejects a significant portion of the signal [26]. An accurate determination of the efficiency from this veto is essential for a reliable measurement of the signal cross section. In this section we provide a detailed description of the Bhabha-mask rejection that selection criterion (9) is based on.

1. Bhabha-veto trigger

A detailed description of the Bhabha trigger (CsiBB) at Belle is given elsewhere [15]. It fires when the energy sum over one- or two-"θ-ring" groups among 11 possible combinations (referred to hereafter as "Logic") is higher than a given threshold. A θ ring is an array of CsI(Tl) crystals in a certain polar angular range covering 2π in

azimuth. A θ-ring combination corresponds to back-to-back Bhabha electrons in that angular range.

The sum of energies over two θ rings is required but the energy can concentrate in either ring. Thus, an event with a single cluster can satisfy the trigger logic even if it has a non-back-to-back topology in the e^+e^- c.m. frame. This vetoes some fraction of the signal in the two-dimensional angular acceptance plane for $(\cos\theta_e, \cos\theta_{\gamma\gamma})$, especially in the forward region where the energies of the electron and photons are relatively high.

2. Bhabha-mask rejection

As mentioned in selection criterion (9), we reject events for which the angular combination $(\cos\theta_e, \cos\theta_{\gamma\gamma})$ falls in the predetermined two-dimensional angular area. We divide the polar-angle region for the selection of an electron and photon system, $-0.6235 < \cos\theta < 0.9481$, that is, $18.53° < \theta < 128.57°$, into 14 subregions with 13 boundaries [27] according to the boundaries of the CsI crystals that belong to different trigger segments. The acceptance plane $(\cos\theta_e, \cos\theta_{\gamma\gamma})$ is then subdivided into 14×14 rectangular cells (see Fig. 2).

We estimate the efficiency of the Bhabha veto in each cell using the trigger simulator, TSIM. The cells that are sensitive to the veto are removed from the selection. The accepted cells are shown in Fig. 2 in yellow. In this figure, we overlap the distribution from the signal MC simulation (shown with the scattered dots), where the Bhabha veto is not applied, but the high-Q^2 contribution is enhanced as compared to the actual distribution. The two-dimensional angular regions for the p-tag and e-tag are separated into the left-lower region and the right-upper region, respectively.

3. Unbiased sample

The HiE trigger is vetoed by the CsiBB trigger. Hence, the "HiE OR CsiBB" data sample, which is triggered by either of them, is completely free from the Bhabha-veto logic. The events triggered by the Bhabha (CsiBB) trigger are recorded after prescaling by a factor of 1/50. These prescaled events are used in the analysis of the π^0 TFF in the region of Q^2 between 4 and 6 GeV^2.

In addition, this sample is very useful to calibrate the energy threshold of the CsiBB trigger as well as to test the trigger simulation of the HiE trigger in which the Bhabha veto is included. These calibrations and the test of the trigger simulation have been carried out by using radiative-Bhabha events $[e^+e^- \to (e)e\gamma]$ in the special configuration where one of the final-state electrons is scattered into the beam pipe. This configuration is usually referred to as VC scattering. The kinematics of VC are very similar to the signal process $[e^+e^- \to (e)e\pi^0]$ so we can use this sample as a calibration signal to validate the trigger simulation using data, which is one of the most important aspects of this analysis.

To compensate for prescaling, we multiply by 50 the number of events recorded by the CsiBB trigger. Thus, to emphasize that the effect of the Bhabha veto is statistically compensated in the complete dataset, it is referred to as "HiE + 50 * CsiBB."

APPENDIX B: CALIBRATION OF THE TRIGGER THRESHOLD

It is necessary to calibrate the trigger thresholds for the Bhabha veto because the inefficiency due to the trigger for the signal is significant. In contrast, the threshold for the HiE trigger is efficient because it is low (around 1.15 GeV) compared to our analysis selection requirement.

There are 11 trigger thresholds for the Bhabha-veto (the same as the CsiBB trigger) and their nominal value is 5.0 GeV, except for Logic#2 (5.5 GeV) and Logic#11 (3.0 GeV) [15]. However, the thresholds determined from Bhabha events in data indicate that the actual values of the thresholds are larger, typically by 0.2 GeV. In addition, the threshold implemented in the TSIM trigger simulator is a step function while the data exhibit the turn-on curves typical for such triggers. We correct for these differences between data and MC.

The trigger efficiency is studied and tuned using radiative-Bhabha $[e^+e^- \to (e)e\gamma]$ events with the VC configuration as described in the next subsection. The radiative-Bhabha cross section in the VC configuration is very large; it is $\mathcal{O}(10^4$–$10^5)$ times larger than the signal process. Significant and sufficient statistics for radiative-Bhabha events are available even in the prescaled CsiBB data samples.

In Sec. B 1, we describe tuning of the Bhabha-veto threshold using an unbiased sample of radiative-Bhabha events, which are compared to events generated by Rabhat MC together with TSIM and GSIM (detector simulator). The Rabhat MC is described in detail in Sec. B 2. Finally, in Sec. B 3, various distributions including Q^2 in data and MC are compared to check the validity of the tuned MC, first for unbiased data and then for HiE triggered data.

1. Tuning of CsiBB thresholds with radiative-Bhabha events

We compare the radiative-Bhabha events in data with the MC events from Rabhat, collected with selection criteria similar to those for the signal process. To select the radiative-Bhabha events, we relax the selection requirements by allowing events with a single photon. The energy requirement for both the electron and photon is slightly more restrictive, greater than 1.5 GeV, in order to collect $(e)e\gamma$ samples with negligible background contamination. The conditions for the angles and the other selection requirements are the same as those in the analysis of the signal process. The three-body kinematical selection is applied assuming a single real photon, $0.85 < E_{\rm ratio} < 1.1$. We define the p- and e-tags and Q^2 in the same manner

as in the measurement of the single-tag two-photon process from the detected electron for each event, although the physics mechanism is different.

We measure the threshold curve for each CsiBB Logic by counting the yields from the two triggers and by forming the ratio

$$y_{\text{ratio}} = \frac{50 * N_{\text{CsiBB}}}{N_{\text{HiE}} + 50 * N_{\text{CsiBB}}} \tag{B1}$$

as a function of the energy sum (E_{sum}) over the electron and photon deposited in a pattern of the Logic for both experimental data and MC, where N_{CsiBB} ($N_{\text{HiE}} + 50 * N_{\text{CsiBB}}$) is the number of events triggered by the CsiBB (HiE + CsiBB multiplied by 50) trigger(s) and the factor of 50 corrects for the prescaling in the CsiBB trigger. Note that, in matching y_{ratio} between data and MC, tuning of the TSIM threshold is essential while the details of the physics simulated by Rabhat are not. We obtain the energy dependence of y_{ratio} for each Logic. We use the energy sum (E_{sum}) over the electron or the photon that enters the relevant ECL θ ring(s) to the Logic. In each Logic, only the events in which the sum of the deposited energy to the corresponding Logic exceeds $E_{\text{max}} - 1$ GeV are used, where E_{max} is the greatest energy deposit in a given Logic (among the 11) in each event.

We obtain the threshold curves for each Logic for data and MC simulation and tune the latter to match the former. We tune the threshold behavior of the MC so that it agrees well with that in data as shown in Fig. 25. The thresholds are thus adjusted with an accuracy better than ± 0.2 GeV. The nonzero efficiency below the nominal threshold is due to an artifact from events that are triggered by a different Logic. The real thresholds are near 5–6 GeV for Logics#1–10 and near 3 GeV for Logic#11. The gaps near 7.5 GeV, when present, correspond to a region almost prohibited by the kinematics of $(e)e\gamma$.

We confirm the result of the tuning and its validity by comparing distributions of the radiative-Bhabha events between the experimental data and MC in Sec. B 3. We use the event yields for this purpose because the radiative-Bhabha cross section is well known.

2. Rabhat, MC code for radiative-Bhabha events

We use the MC simulation program Rabhat [16] to generate events with a virtual Compton configuration. Rabhat simulates the radiative-Bhabha process with a t-channel mass singularity. This singularity occurs in a topology in which the virtual photon that is emitted at an extremely forward angle from one of the incident electrons is hard scattered off the other electron. Although the cross section is finite and is not very large, our requirement of an energetic final-state photon at a finite angle results in a relatively sharp mass singularity for an acoplanarity angle of order E_γ/m_e. Rabhat adopts a careful choice of integration variables and a proper technique for numerical integration. We used Rabhat to simulate approximately 2×10^8 (3.6×10^7) MC events for $\sqrt{s} = 10.58$ GeV (10.88 GeV). A limitation of Rabhat is that it calculates the lowest order $e^+e^- \to e^+e^-\gamma$ process [$\mathcal{O}(\alpha^3)$]. There could be an uncertainty from radiative corrections, typically of order 5%, which is estimated from the size of the radiative correction $1 + \delta$ for the Compton process, $e\gamma \to e\gamma$, where $\delta \sim -6\%$ in the similar $e\gamma$ c.m. energy region (around 3–10 GeV) [28].

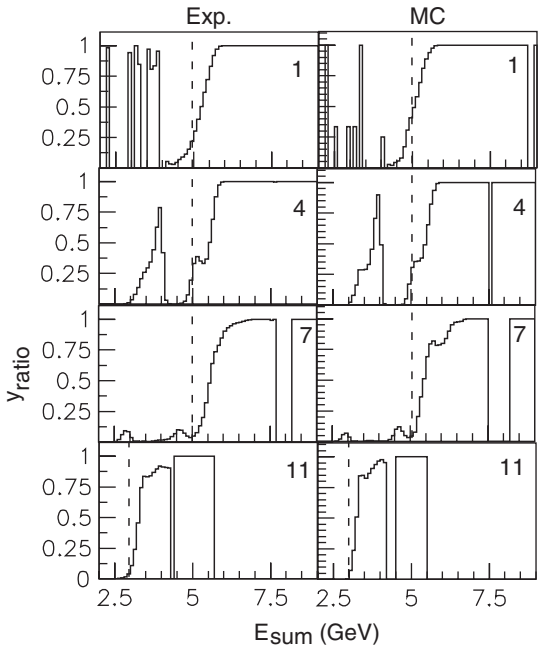

FIG. 25. The threshold behavior for the four selected Logics of the CsiBB trigger (identified in each subfigure) obtained from the experimental samples (left column) of radiative-Bhabha events and from the MC events, where the trigger simulator is tuned (right column). The dashed lines show the position of the nominal trigger thresholds.

3. Comparison between the data and MC for radiative-Bhabha events

In this subsection, we first compare experimental data for the HiE + 50 * CsiBB sample with MC, where the CsiBB threshold effect is absent, to show that MC can reproduce various distributions fairly well (Figs. 26 and 27). Similar plots are presented for the HiE triggered events (Figs. 28 and 29) to show that the agreement between data and MC is also adequate. We use an MC sample where the CsiBB threshold is tuned as described in Sec. B 1. We then show the HiE-trigger efficiency determined by data using radiative-Bhabha events and compare it to the results from the trigger simulation (Fig. 30).

We show the comparison in distributions for polar angles of the photon and electron, energy-sum and cell pattern as correlation of the angles in Fig. 26 for the sample of HiE + 50 * CsiBB. The MC events are normalized to the nominal

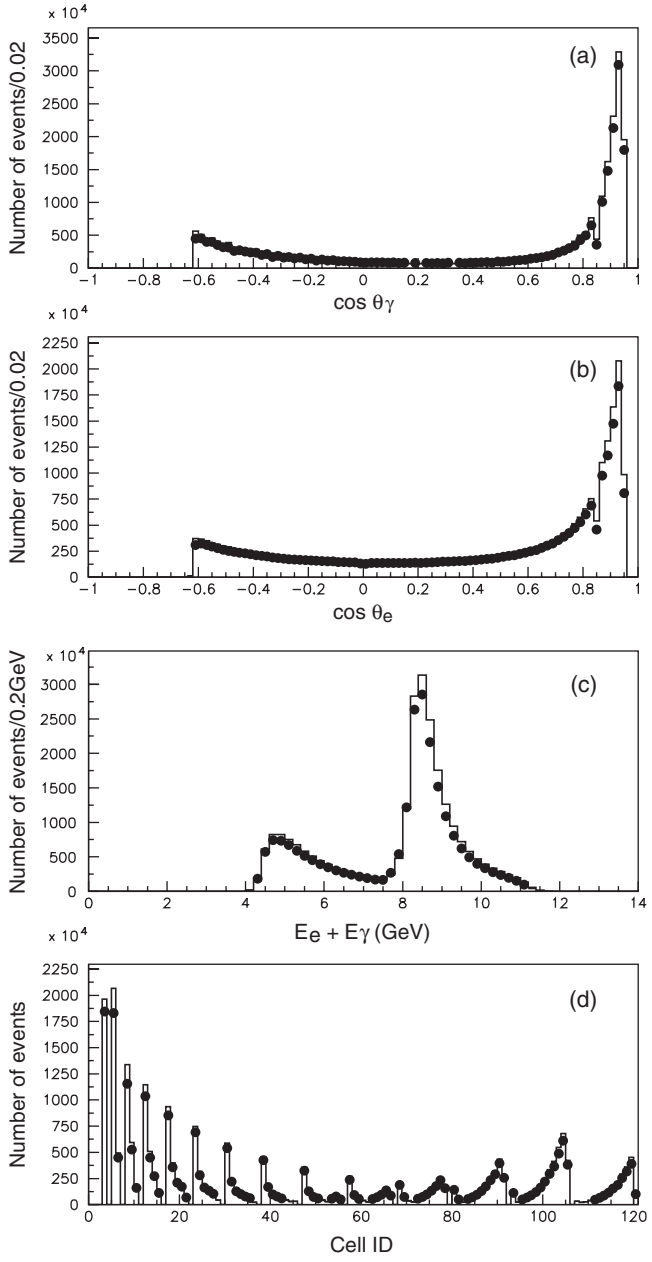

FIG. 26. Comparison of the experimental radiative-Bhabha samples (dots) and the corresponding MC (Rabhat, histogram) normalized to the integrated luminosity, triggered by HiE or CsiBB, where the Bhabha mask is not applied. The distributions are (a) polar angle of the photon, (b) polar-angle of the electron, (c) sum of the photon and electron energies, and (d) identification number of the cell in the $(\cos\theta_e, \cos\theta_\gamma)$ plane.

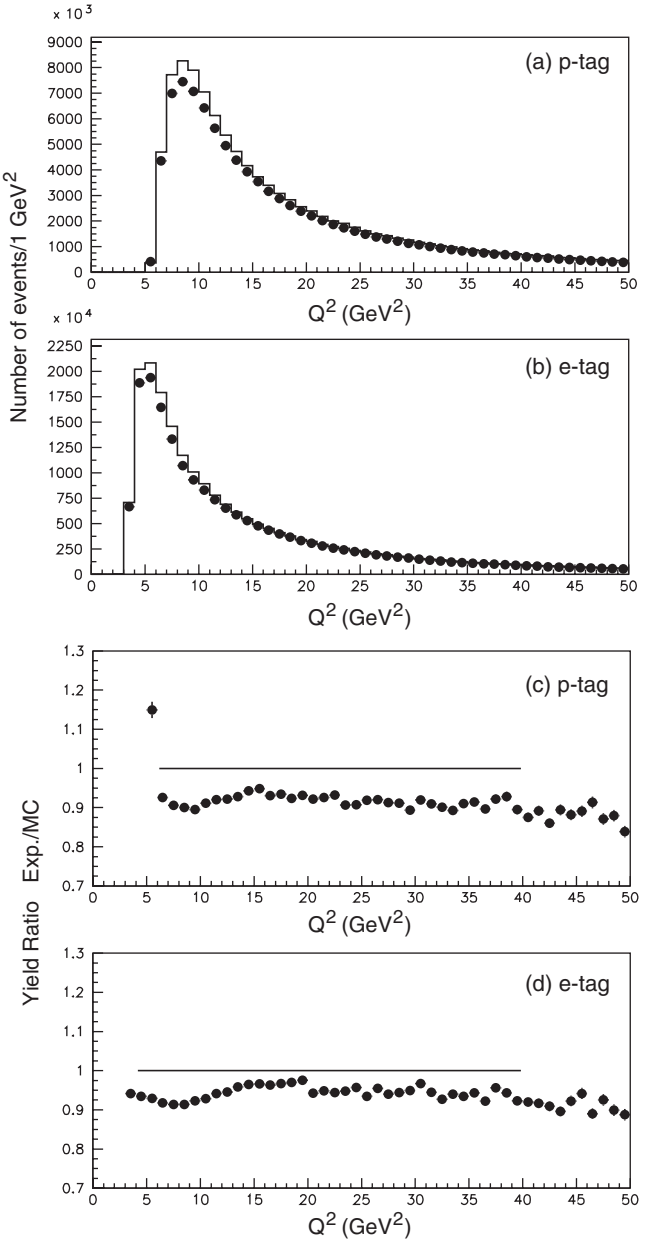

FIG. 27. (a), (b) Comparison of the experimental radiative-Bhabha samples (dots) and the corresponding MC (Rabhat, histogram) normalized to the integrated luminosity, triggered by HiE or CsiBB, where the Bhabha mask is not applied, for the Q^2 distributions of the detected electron, where the two selection criteria related to the p_t balance are loosened (see the text). (c), (d) The ratio of the experimental yield to the normalized MC yield. The sizes of the vertical error bars correspond to the statistical errors in both experimental and MC samples. The horizontal lines at 1.0 show the Q^2 region where the measurement of the π^0 TFF is performed.

luminosity; radiative corrections are included in this normalization. The horizontal axis for the cell identification number corresponds to each cell in the $(\cos\theta_e, \cos\theta_\gamma)$ plane in which the symmetry in interchanging $\cos\theta_e$ and $\cos\theta_\gamma$ is taken into account (see Fig. 2).

The Q^2 distributions for data and MC for the unbiased sample (HiE + 50 * CsiBB) are shown in Figs. 27(a) and 27(b) for the p- and e-tag samples, respectively. Figures 27(c) and 27(d) are the ratio between data and MC for the p- and e-tag separately. In these comparisons, we include the radiative correction of $\delta = -6\%$ and loosen the selection criteria related to the p_t balance

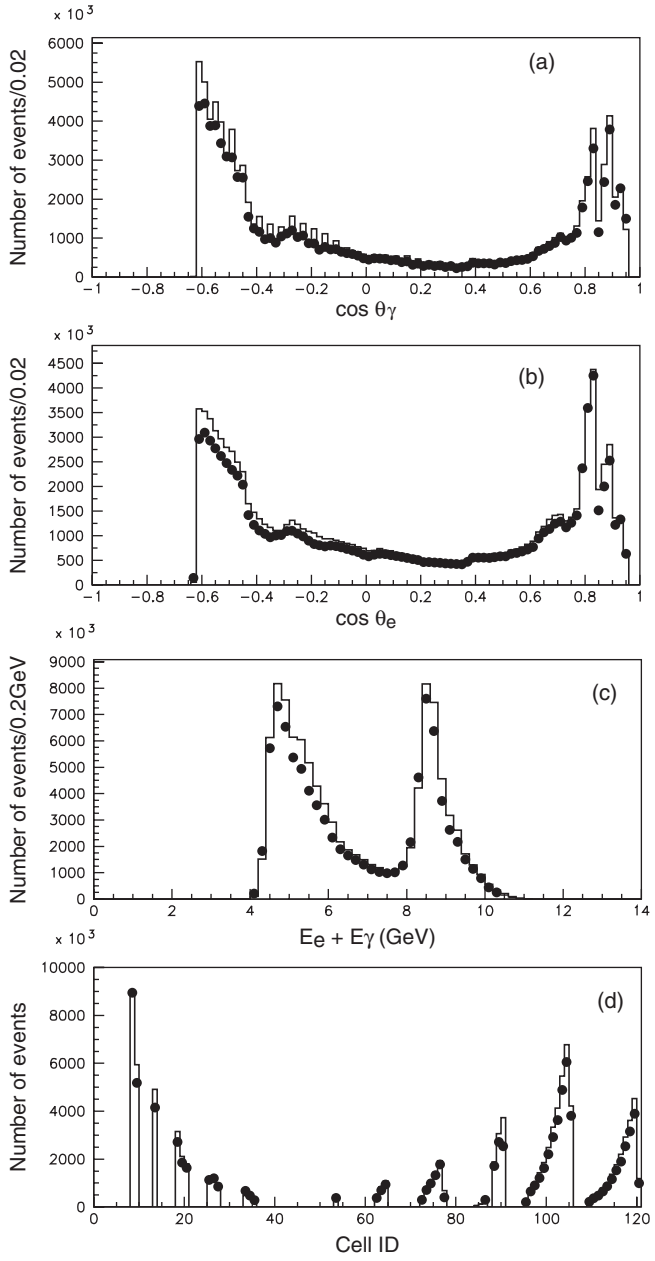

FIG. 28. Comparison of the experimental radiative-Bhabha samples (dots) and the corresponding MC (Rabhat, histogram) normalized to the integrated luminosity, triggered by HiE, where the Bhabha mask and veto are applied. See the caption of Fig. 26 for more information.

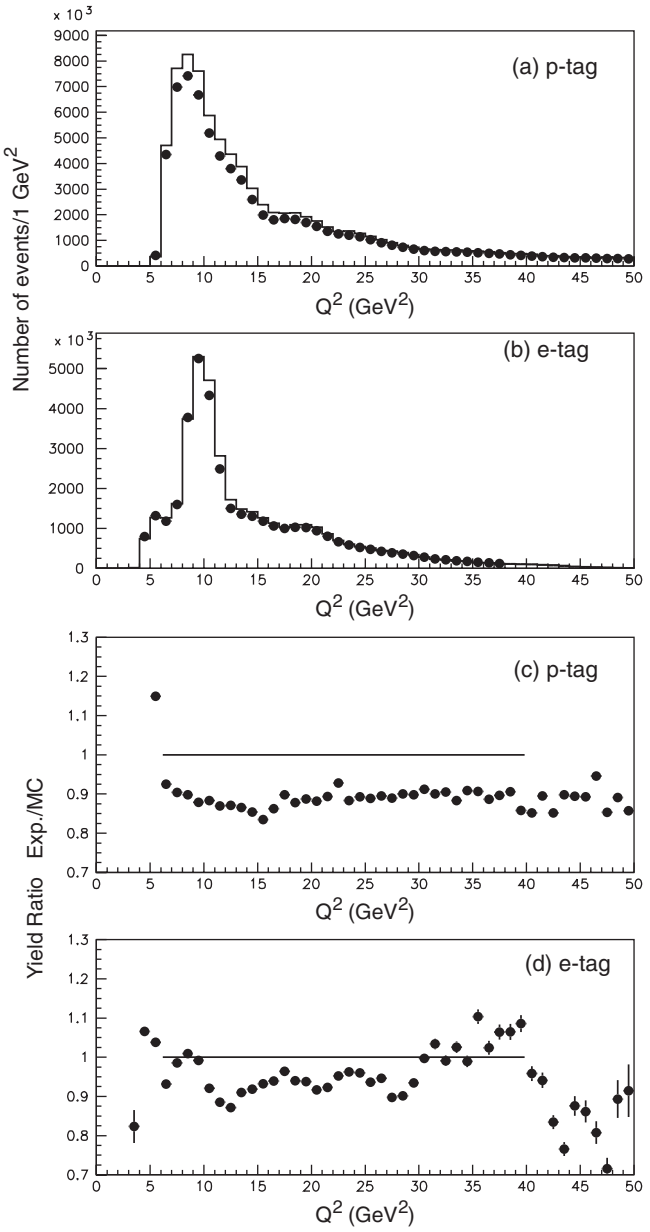

FIG. 29. Comparison of the experimental radiative-Bhabha samples (dots) and the corresponding MC (Rabhat, histogram) normalized to the integrated luminosity, triggered by HiE, where the Bhabha mask and veto are applied. See the caption of Fig. 27 for each figure. The horizontal lines at 1.0 in (c), (d) show the Q^2 region where the measurement of the π^0 TFF is performed using HiE-trigger data.

conditions for the $e\gamma$ system to $\alpha(e, \gamma) < 0.3$ radians and $|\Sigma \boldsymbol{p}_t^*| < 0.5$ GeV$/c$, for a more meaningful comparison of the yield, noting that the p_t balance is affected by the emission of an extra photon; the effect is typically 4%.

Figures 28 and 29 present similar distributions for the samples after applying TSIM for the HiE trigger including applications of the Bhabha veto and Bhabha mask. The results agree to within the 5%–10% level [Figs. 29(c) and 29(d)]. A deficit of events is seen in both the p-tag and e-tag modes, and also in the HiE + 50 $*$ CsiBB sample [Figs. 27(c) and 27(d)]. This discrepancy is not due to the Bhabha veto, because a deficit of similar size is also seen in the regions where the veto has little or no inefficiency, e.g., for $Q^2 < 10$ GeV^2 with the p-tag. Moreover, the deficits are of similar size in the unbiased sample and in the HiE-trigger sample. These deficits could be due to the uncertainty of the radiative correction δ (4%), an uncertainty in the efficiency due to additional multiphoton emission,

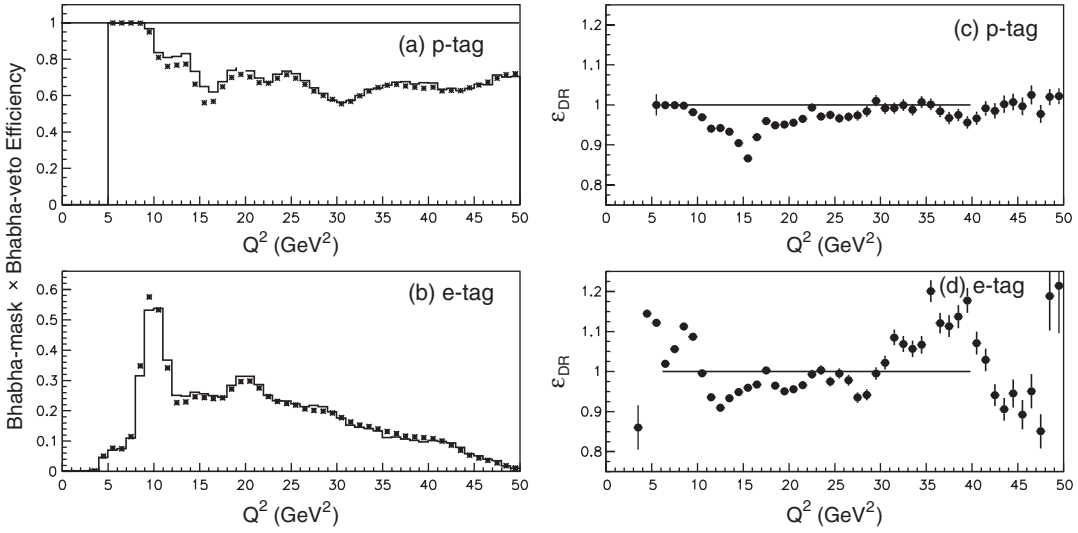

FIG. 30. (a), (b) Comparison between the efficiency of the "Bhabha-mask × Bhabha-veto" for the radiative-Bhabha samples [dots, $x_{\rm ratio}$(data) described in the text] and the corresponding MC [Rabhat, histogram, $x_{\rm ratio}$(MC)] for (a) p-tag and (b) e-tag events. (c), (d) Ratio ($\epsilon_{\rm DR}$) of the efficiencies which are plotted in (a), (b) for the radiative-Bhabha samples and the corresponding MC for (c) p-tag and (d) e-tag events. The vertical error size is derived from the statistical errors in both experimental and MC samples. The horizontal lines at 1.0 show the Q^2 region where the measurement of the π^0 TFF is performed using the Bhabha mask and Bhabha veto.

which is not accounted for in the Rabhat MC (4%), as well as the experimental measurement itself ($\sim 5\%$, similar to the Q^2-independent systematic uncertainty in the efficiency for the signal process in Sec. V E), which amounts to $\sim 8\%$ in total.

The ratio $x_{\rm ratio}$, defined as

$$x_{\rm ratio} = \frac{N_{\rm HiE}}{N_{\rm HiE} + 50 * N_{\rm CsiBB}}, \tag{B2}$$

i.e., the number of events triggered by HiE divided by those triggered by "HiE OR CsiBB," provides the fraction of the events that survive the Bhabha veto. The Bhabha mask is (is not) applied to the HiE (HiE + 50 ∗ CsiBB) sample. Thus, $x_{\rm ratio}$ contains the effect of the Bhabha mask as an inefficiency. Note that this ratio is not affected by uncertainties in normalization such as those coming from the radiative corrections of the Bhabha generators as well as that from the experimental measurements. The ratio $x_{\rm ratio}$ is shown as a function of Q^2 for the data and Rabhat MC events tagged by positrons and electrons in Figs. 30(a) and 30(b), respectively. The double ratio ($\epsilon_{\rm DR}$) between data and MC

$$\epsilon_{\rm DR} = \frac{x_{\rm ratio}({\rm data})}{x_{\rm ratio}({\rm MC})}, \tag{B3}$$

shown in Figs. 30(c) and 30(d), demonstrates that the Bhabha-veto efficiency simulated by the MC agrees with data to within ±(5%–10%).

[1] B. Aubert *et al.* (*BABAR* Collaboration), Phys. Rev. D **80**, 052002 (2009).
[2] P. del Amo Sanchez *et al.* (*BABAR* Collaboration), Phys. Rev. D **84**, 052001 (2011).
[3] H. J. Behrend *et al.* (CELLO Collaboration), Z. Phys. C **49**, 401 (1991).
[4] J. Gronberg *et al.* (CLEO Collaboration), Phys. Rev. D **57**, 33 (1998).
[5] G. P. Lepage and S. J. Brodsky, Phys. Rev. D **22**, 2157 (1980).
[6] S. S. Agaev, V. M. Braun, N. Offen, and F. A. Porkert, Phys. Rev. D **83**, 054020 (2011); we follow the notation in this reference.
[7] A. V. Radyushkin, Phys. Rev. D **80**, 094009 (2009).
[8] M. V. Polyakov, JETP Lett. **90**, 228 (2009).
[9] T. N. Pham and X. Y. Pham, Int. J. Mod. Phys. A **26**, 4125 (2011).
[10] S. V. Mikhailov and N. G. Stefanis, Mod. Phys. Lett. A **24**, 2858 (2009).
[11] H. L. L. Roberts, C. D. Roberts, A. Bashir, L. X. Gutiérrez-Guerrero, and P. C. Tandy, Phys. Rev. C **82**, 065202 (2010).
[12] S. J. Brodsky, F.-G. Cao, and G. F. de Téramond, Phys. Rev. D **84**, 033001 (2011); **84**, 075012 (2011); most of the earlier theoretical attempts are listed in these articles.

[13] S. Kurokawa and E. Kikutani, Nucl. Instrum. Methods Phys. Res., Sect. A **499**, 1 (2003), and other papers included in this volume.
[14] A. Abashian *et al.* (Belle Collaboration), Nucl. Instrum. Methods Phys. Res., Sect. A **479**, 117 (2002).
[15] B. G. Cheon *et al.*, Nucl. Instrum. Methods Phys. Res., Sect. A **494**, 548 (2002).
[16] K. Tobimatsu and Y. Shimizu, Comput. Phys. Commun. **55**, 337 (1989).
[17] S. J. Brodsky, T. Kinoshita, and H. Terazawa, Phys. Rev. D **4**, 1532 (1971).
[18] S. Uehara, KEK Report No. 96-11 (1996).
[19] G. A. Schuler, Report No. CERN-TH/96-297 (1996).
[20] E. Etim, G. Pancheri, and B. Touschek, Nuovo Cimento B **51**, 276 (1967).
[21] V. P. Druzhinin, L. A. Kardapoltsev, and V. A. Tayursky, arXiv:1010.5969.
[22] H. Genzel *et al.*, *Landolt-Börnstein: Numerical Data and Functional Relationships in Science and Technology*, New Series, Group I Vol. 8 (Springer, Berlin, 1973), p. 314.
[23] S. Uehara, Y. Watanabe, H. Nakazawa *et al.* (Belle Collaboration), Phys. Rev. D **79**, 052009 (2009).
[24] J. J. Sakurai and D. Schildknecht, Phys. Lett. **40B**, 121 (1972); A. M. Breakstone, D. Cheng, D. Dorfan, A. Grillo, C. Heusch, V. Palladino, T. Schalk, A. Seiden, and D. Smith, Phys. Rev. Lett. **47**, 1782 (1981).
[25] S. Ong and P. Kessler, Phys. Rev. D **38**, 2280 (1988); M. Benayoun, S. I. Eidelman, V. N. Ivanchenko, and Z. K. Silagadze, Mod. Phys. Lett. A **14**, 2605 (1999); F. Jegerlehner, J. Phys. G **29**, 101 (2003).
[26] This contrasts with *BaBar* where a special trigger was made available for the signal [1,2].
[27] At 25.95°, 32.27°, 37.81°, 44.17°, 51.39°, 59.42°, 68.24°, 77.73°, 87.68°, 97.36°, 107.10°, 116.27°, and 124.73°.
[28] K. J. Mork, Phys. Rev. A **4**, 917 (1971).